RMetS

Royal Meteorological Society

The Flux-Form Semi-Lagrangian Spectral Element (FF-SLSE) method for tracer transport

Paul A. Ullrich[a]* and Matthew R. Norman[b]†

[a]*University of California, Davis, California, USA*
[b]*Oak Ridge National Laboratory, Tennessee, USA*

*Correspondence to: Paul Ullrich, Department of Land, Air and Water Resources, University of California, One Shields Avenue, Davis, CA 95616, USA. E-mail: paullrich@ucdavis.edu
†The contribution of M. R. Norman to this article was prepared as part of his official duties as a US Federal Government employee.

The spectral element dynamical core has been demonstrated to be an accurate and scalable approach for solving the equations of motion in the atmosphere. However, it is also known that use of the spectral element method for tracer transport is costly and requires substantial parallel communication over a single time step. Consequently, recent efforts have turned to finding alternative transport schemes which maintain the scalability of the spectral element method without its significant cost. This article proposes a conservative semi-Lagrangian approach for tracer transport which uses upstream trajectories to solve the transport equation on the native spectral element grid. This formulation, entitled the Flux-Form Semi-Lagrangian Spectral Element (FF-SLSE) method, is highly accurate compared to many competing schemes, allows for large time steps, and requires fewer parallel communications over the same time interval than the spectral element method. In addition, the approach guarantees local conservation and is easily paired with a filter which can be used to ensure positivity. This article presents the dispersion relation for the 1D FF-SLSE approach and demonstrates stability up to a Courant number of 2.44 with cubic basis. Several standard numerical tests are presented for the method in 2D to verify correctness, accuracy and robustness of the method, including a new test of a divergent flow in Carteisan geometry.

Key Words: high-order; tracer transport; semi-Lagrangian; spectral element method; finite element method

1. Introduction

Tracer transport is one of the most important components of any atmospheric model. Atmospheric chemistry, radiative transfer and cloud physics all rely heavily on accurate transport of tracer species by the dynamical core. Although tracer transport is easy to formulate mathematically, a physical treatment of tracer variables imposes additional constraints such as conservation and positivity. Further, an accurate treatment of the transport equation is often difficult to achieve without a corresponding loss in efficiency. Overall, the challenges with a correct treatment of the transport equation can be quite imposing (Lauritzen *et al.*, 2011b).

Semi-Lagrangian methods cover a wide class of methods which aim to translate many advantages of fully Lagrangian schemes into an Eulerian context. Since tracer concentrations are constant along characteristics, the Lagrangian treatment is perhaps the most natural for tracer advection. Semi-Lagrangian methods can be thought of as Lagrangian schemes which, at the end of each discrete time step, are remapped to a static reference grid. For semi-Lagrangian methods the tracking of individual fluid parcels over many time steps, as required in the Lagrangian approach, is unnecessary. Further, for a sufficiently small time step, semi-Lagrangian approaches maintain locality over the duration of one time step, and so have the potential to scale well on large-scale parallel computer systems. Outside of the meteorological literature, semi-Lagrangian methods are known as Arbitrary Lagrangian–Eulerian methods (Hirt *et al.*, 1974).

Within the regime of geophysical flows, semi-Lagrangian methods have been favoured for over two decades (Staniforth and Côté, 1991). Although classical non-conservative semi-Lagrangian formulations are well-known, more recent conservative semi-Lagrangian schemes have been featured heavily in the literature. Among conservative schemes, remap-based semi-Lagrangian schemes have been demonstrated to be a powerful tool for modelling tracer transport. These methods appear as either upstream or downstream semi-Lagrangian methods: upstream semi-Lagrangian methods track control volumes upstream over one time step and conservatively remap element averages from the reference grid onto the deformed mesh, whereas downstream semi-Lagrangian methods track control volumes downstream and remap from the deformed mesh to the reference grid. The stability of these formulations depends largely on the flow field and the corresponding trajectory tracking algorithm, and the time step must

typically be chosen small enough to avoid crossed trajectories. These schemes also tend to be difficult to extend beyond 2D due to the increased complexity of the deformed mesh in higher dimensions. One of the earliest remap-based approaches is the scheme of Rančic (1992), hereafter R92, which employs a bi-parabolic extension of the piecewise parabolic method (PPM) of Colella and Woodward (1984) and approximates upstream control volumes as deformed quadrilaterals. The relative mathematical complexity of this approach (and the difficulty of extending this approach to 3D) led to the development of simplified approaches, such as the scheme of Laprise and Plante (1995) which instead tracks back the centrepoints of Eulerian element edges to obtain simplified upstream quadrilaterals. To simplify remapping in 2D and beyond, the cascade remapping procedure of Purser and Leslie (1991) approximates upstream control volumes by using grid-aligned slices in each of the 'cascade directions'. This procedure has been applied in the formulation of Leslie and Purser (1995), and extended by Zerroukat *et al.* (2002) as part of the SLICE scheme (and on the latitude–longitude grid by Zerroukat *et al.*, 2004). Cascade remapping is also covered in the work of Nair *et al.* (2002) and Norman and Nair (2008). Recent work by Lauritzen *et al.* (2010) has introduced the CSLAM scheme, which extends the R92 approach to the cubed-sphere grid with a truncated subgrid-scale reconstruction. For each of these methods, the use of straight lines to approximate upstream control volumes limits the formal accuracy of these methods to second-order, although a modification by Ullrich *et al.* (2012) has been introduced to extend CSLAM to third-order. Shape-preservation in remapping schemes is easily obtained by using a slope limiter procedure, such as the one by Barth and Jespersen (1989).

Although remap-based methods have been very successful in modelling tracer transport, the conservative remapping procedure is often both complicated and costly. Consequently, flux-form semi-Lagrangian (FF-SL) methods were developed which implicitly guarantee conservation regardless of the choice of flux. One of the earliest FF-SL approaches has been proposed by Leonard *et al.* (1996), which describes a novel dimension-splitting technique for combining 1D semi-Lagrangian operators to build conservative 2D and 3D transport schemes, although the dimension-splitting technique formally limits the accuracy of the method to second-order. Further, the lack of true multi-dimensionality adversely affects the accuracy of this method for large values of the Courant number. A similar approach has been proposed by Lin and Rood (1996), which essentially applies 1D PPM in each of the coordinate directions. This formulation features improved accuracy compared with the piecewise linear reconstructions, especially for flows which are aligned with the grid and, although the formal accuracy is still limited to second-order, this method has been an important driver of the use of FF-SL methods in the atmospheric sciences. By using dimension-splitting, these methods can easily achieve unconditional stability, which is considerably more difficult for multi-dimensional schemes. For instance, FF-SL methods have been extended onto unstructured grids by Frolkovič (2002), although the multidimensional application of these flux-based methods also led to a loss of unconditional stability and restricted the Courant number to $\nu \leq 1$. The CSLAM scheme has been presented in flux-form by Harris *et al.* (2011) using the full intersection search algorithm, and consequently the results were identical to the original CSLAM formulation. A relaxed formulation is described in Lauritzen *et al.* (2011a), which simplifies the flux calculation by only using the subgrid-scale reconstruction in elements that bounded each flux-edge. However, simplification of the flux calculation also leads to a stability constraint of approximately $\nu \leq 1$. Shape preservation in flux-form semi-Lagrangian schemes is typically attained via flux-corrected transport (FCT; Zalesak, 1979).

Recent efforts dedicated to the development of next-generation atmospheric dynamical cores have focused on finite-element methods for achieving parallel scalability on supercomputers with hundreds of thousands of processor cores. The spectral element method (SEM; Patera, 1984; Maday and Patera, 1989) has several important properties that make it a desirable choice for atmospheric dynamics including conservation of mass and energy, flexibility and accuracy. This approach was first adopted in the ocean modelling community by Ma (1993) and later for shallow-water simulations on the sphere by Taylor *et al.* (1997). More recently, the spectral element method has been implemented as an atmospheric dynamical core (Fournier *et al.*, 2004; Taylor and Fournier, 2010) and is now included as part of the Community Atmosphere Model (CAM) as the default dynamical core (Dennis *et al.*, 2012). A regional modelling environment using both the spectral element and discontinuous Galerkin methods has also been developed (Giraldo and Rosmond, 2004; Giraldo and Restelli, 2008). Within CAM, SEM is currently used for both the thermodynamical component of the atmospheric model (which handles pressure, velocity and temperature) and the advective component (for all other tracer species). However, this scheme has known shortfalls for tracer advection, including a fairly strict CFL condition which limits the maximum time step and a requirement for several parallel communications within every time step. Consequently new algorithms for tracer transport within the spectral element dynamical core are desired.

A variety of semi-Lagrangian methods have been developed for the general class of finite-element and multi-moment methods. One of the earliest known methods is the remapping scheme of Prather (1986) (hereafter P86), which preserves second moments of the tracer distribution within each element (quadratic polynomials) while maintaining unconditional stability. This scheme assumes no deformation of the fluid parcel over the duration of the time step, which tends to be the dominant form of error of this scheme. This method can also be applied in a direction-split context, and tends to perform better than analogous dimension-split finite-volume schemes. Increased interest in finite-element methods later followed from the work of Cockburn and Shu (1989). A nodal semi-Lagrangian spectral element method for tracer transport was introduced by Giraldo (1998) (hereafter G98), and although this method was unconditionally stable and allowed for arbitrary order-of-accuracy, the use of the advective form of the transport equation did not lead to strict tracer mass conservation. This work was later extended to the spherical shallow-water equations by Giraldo *et al.* (2003) and the Navier–Stokes equations by Xiu and Karniadakis (2001).

Recent work by Restelli *et al.* (2006) (hereafter RBS06) has introduced a semi-Lagrangian discontinuous Galerkin method analogous to the multi-dimensional approach of P86 which is valid for unstructured grids and arbitrary order-of-accuracy. Further, RBS06 presents a mechanism for enforcing shape preservation within the formulation via FCT. RBS06 relates most closely to the efforts in this article, although they make a number of assumptions in their derivation which are not imposed herein, including incompressibility of the velocity field ($\nabla \cdot \mathbf{u} = 0$), constancy of the flow field over the duration of one time step, and orthogonality of test functions (leading to a diagonal mass matrix). Further, RBS06 limits their stability analysis to methods of second-order accuracy and provides results for schemes only up to third-order.

The space of semi-Lagrangian finite-element methods remains to be fully explored, and so the goal of this article is to build on the earlier work by G98 and RBS06 to construct a transport scheme which is compatible with the fourth-order nodal spectral element method of Fournier *et al.* (2004), and hence is appropriate for incorporation in CAM. In particular, to be useful operationally, such a scheme should possess the following properties:

1. Uses the native spectral element nodal grid,
2. Conserves mass without *a posteriori* mass fixers,
3. Allows for at least third-order accuracy,
4. Maintains stability up to a Courant number of 1,
5. Maintains strict positivity of the tracer field.

The Flux-Form Semi-Lagrangian Spectral Element (FF-SLSE) method described in this article also has several desirable properties. Since this scheme is formulated in flux-form, local and global conservation of tracer mass is immediately guaranteed. Similar to SEM, FF-SLSE also admits both a variational formulation and finite-difference formulation. This article further demonstrates that positivity can be maintained using a modified FCT method analogous to the approach of RBS06. The FF-SLSE method also becomes more cost effective per tracer as the number of tracers increases, since the trajectory tracking algorithm needs to be performed only once for each time step. This advantage is especially beneficial going forward, since version 5 of CAM now runs with roughly 30 tracers in operational mode, and up to 106 with the full chemistry suite. As formulated, FF-SLSE is unstable with cubic basis functions (fourth-order accuracy), but can be stabilized with a selectively chosen ∇^4 hyperdiffusion operator, which ensures third-order accuracy and is stable up to a 1D Courant number of 2.44. This CFL condition leads to a scheme which requires significantly fewer parallel communications per unit time than SEM. Unlike many other semi-Lagrangian schemes, it is worthwhile to emphasize that unconditional stability is not guaranteed under FF-SLSE, which may make the scheme unattractive, especially when coupled with a scheme for the thermodynamic variables which allows for large time steps. However, to achieve massive parallel scalability with a CFL-limited numerical approach (such as the default for the CAM-SE dynamical core), one typically requires communication locality (Dennis *et al.*, 2012), and so computational considerations effectively limit the value of the Courant number to not be 'too large' to require extra communication.

The outline of this article is as follows. Section 2 outlines the FF-SLSE method, including the description of the hyperdiffusion operator and the positivity filter. An analysis of the dispersive properties of the fourth-order method in 1D is performed in section 3. A suite of 2D numerical tests are then performed in section 4 to verify the theoretical properties of the method. Finally, conclusions and future work are presented in section 5.

2. The Flux-Form Semi-Lagrangian Spectral-Element (FF-SLSE) method

2.1. Spectral elements and Gauss−Lobatto−Legendre characteristic functions

The 1D Gauss−Lobatto−Legendre (GLL) characteristic functions are based on the nodal Gauss−Lobatto grid. Consider a 1D reference element on the closed interval $[-1, 1]$. For a given polynomial degree $n_p \geq 1$, the nodal Gauss−Lobatto points include both endpoints $\widetilde{x}_1 = -1$ and $\widetilde{x}_{n_p+1} = 1$ and $n_p - 1$

interior nodes, defined by the roots of $P'_{n_p-1}(\widetilde{x})$, where P_n is a Legendre polynomial. This choice leads to an implied quadrature rule over $[-1, 1]$ with corresponding nodal weights

$$w_i = \frac{2}{n_p(n_p - 1)[P_{n_p-1}(\widetilde{x}_i)]^2}. \tag{1}$$

The ith GLL characteristic function on this grid is defined as the lowest-order polynomial which is 1 at $\widetilde{x}_i$ and 0 at all $\widetilde{x}_j$ with $j \neq i$. This article is primarily interested in methods which use third-degree (cubic) polynomials within each spectral element, consistent with the typical order of the CAM-SE dynamical core. A depiction of this reference element and its corresponding characteristic functions is given in Figure 1. When using quadrilateral (2D) and hexahedral (3D) spectral elements, the characteristic functions in 1D can be easily extended to higher dimensions via a tensor product. In the global domain, which consists of an appropriate tiling of spectral elements, nodal points are labelled using vector notation $\mathbf{x}_j$ where the index j spans all nodes.

The spectral element method, and consequently the FF-SLSE method, further enforce continuity at element boundaries. The characteristic functions which are non-zero at element boundaries are mirrored in immediate neighbours to give an overlapping set of basis functions. This requirement also implies that any degrees of freedom at element boundaries are shared between spectral elements. Hence, each element contains one fewer degree of freedom than its number of basis functions (three degrees of freedom per spectral element for cubic basis functions). The basis function $\phi_j(\mathbf{x})$ is then defined as the characteristic function (or mirrored characteristic function) which is 1 at $\mathbf{x}_j$ and 0 at all other nodes.

2.2. Variational formulation of the spectral element method

For simplicity, the spatial domain $\mathcal{D}$ is assumed to be periodic in all coordinate directions. The conservative form of the advection equation is written as

$$\frac{\partial \psi}{\partial t} + \nabla \cdot \mathbf{F}(\psi; \mathbf{u}) = 0, \tag{2}$$

where $\psi = \rho q = \psi(\mathbf{x}, t)$ is a tracer density variable composed of the density ρ and tracer concentration q, $\mathbf{u} = \mathbf{u}(\mathbf{x}, t)$ is a specified velocity field and $\mathbf{F}(\psi; \mathbf{u}) = \psi \mathbf{u}$. The tracer density ψ is approximated using a basis function expansion,

$$\psi(\mathbf{x}, t) = \sum_j \psi_j(t)\, \phi_j(\mathbf{x}), \tag{3}$$
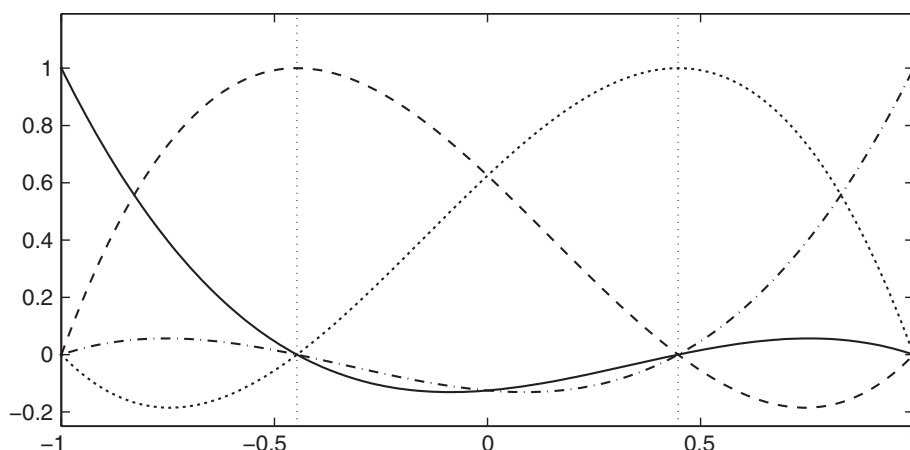
Figure 1. A depiction of the four GLL basis functions associated with the reference element $[-1, 1]$. The vertical dotted lines indicate the roots of the Legendre polynomial P_3.

where the sum is taken over the full set of basis functions and $\psi_j(t) = \psi(\mathbf{x}_j, t)$. The differential equation is multiplied by $\phi_i(x)$ and integrated over $\mathcal{D}$, which leads to

$$\sum_{j=1}^{N} \frac{d\psi_j}{dt} \int_{\mathcal{D}} \phi_i(\mathbf{x})\,\phi_j(\mathbf{x})\,dV = -\int_{\mathcal{D}} \phi_i(\mathbf{x}) \nabla \cdot \mathbf{F}(\psi;\mathbf{u})\,dV, \quad (4)$$

where the boundary integral term is dropped due to periodicity of $\mathcal{D}$ and dV is the volume element associated with $\mathcal{D}$. Under the Galerkin formulation, this equation must be satisfied for all basis functions ϕ_i. Integration by parts is now applied to obtain the weak form,

$$\sum_{j=1}^{N} \frac{d\psi_j}{dt} \int_{\mathcal{D}} \phi_i(\mathbf{x})\,\phi_j(\mathbf{x})\,dV = \int_{\mathcal{D}} \mathbf{F}(\psi;\mathbf{u}) \cdot \nabla \phi_i(\mathbf{x})\,dV. \quad (5)$$

In matrix form, this system of equations can be written as

$$\mathbf{M}\frac{d\boldsymbol{\psi}}{dt} = \mathbf{G}, \quad (6)$$

where $\boldsymbol{\psi} = \boldsymbol{\psi}(t) = [\psi_j(t)]_{j=1}^{N}$ is the vector of nodal values, $\mathbf{M}$ is the symmetric mass matrix with components

$$(\mathbf{M})_{ij} = \int_{\mathcal{D}} \phi_i(\mathbf{x})\phi_j(\mathbf{x})\,dV, \quad (7)$$

and $\mathbf{G}$ is the vector of integrated fluxes,

$$\mathbf{G}_i = \int_{\mathcal{D}} \mathbf{F}(\psi;\mathbf{u}) \cdot \nabla \phi_i(\mathbf{x})\,dV. \quad (8)$$

If the integrals in (7) are evaluated exactly, the global system of equation (6) must be inverted at each time step. However, in this article all integrals are instead evaluated using the Gauss–Lobatto integration rule induced by the underlying grid. Using this approach, the mass matrix will be diagonal and the inversion will no longer require a global matrix-vector solve. This technique is also known as mass-lumping, since it is identical to replacing $\mathbf{M}$ with a diagonal matrix composed of the row sums of $\mathbf{M}$. Another advantage of this technique is that fluxes must only be computed at GLL points, since each component of the flux vector (8) will reduce to a weighted sum of pointwise fluxes.

It should be emphasized that the discretization (6)–(8) is inherently conservative for any choice of flux function $\mathbf{F}$. This property makes it possible to guarantee global mass conservation without the need for *a posteriori* mass fixers.

2.3. Semi-Lagrangian time integration

Equation (6) represents a semi-discrete system of equations. In order to fully discretize these equations, it remains to specify a discretization of the temporal term, which is typically achieved via some appropriately chosen Runge–Kutta method. This work instead uses a semi-Lagrangian discretization, which requires coupling of the spatial and temporal modes. By integrating (6) in time over the interval $\mathcal{T}^n = [t^n, t^{n+1}]$, one obtains the linear system

$$\left[\mathbf{M}\left(\widetilde{\boldsymbol{\psi}}^{n+1} - \boldsymbol{\psi}^n\right)\right]_i = \int_{\mathcal{D}} \overline{\mathbf{F}}^n(\mathbf{x}) \cdot \nabla \phi_i(\mathbf{x})\,dV, \quad (9)$$

with unknown advected tracer density $\widetilde{\boldsymbol{\psi}}^{n+1} = \widetilde{\boldsymbol{\psi}}(t^{n+1})$ and time-integrated pointwise flux

$$\overline{\mathbf{F}}^n(\mathbf{x}) = \int_{\mathcal{T}^n} \mathbf{F}(\psi;\mathbf{u})\,dt. \quad (10)$$

The key to the semi-Lagrangian formulation is in specifying the time-integrated flux (10) using known information. For consistency with the induced quadrature rule on the spatial grid, Gauss–Lobatto quadrature is used to approximate the integral (10), although any other appropriately chosen quadrature rule can also be used. Under this approach, $\overline{\mathbf{F}}^n(\mathbf{x})$ takes the form

$$\overline{\mathbf{F}}^n(\mathbf{x}) = \frac{\Delta t}{2} \sum_{m=1}^{M_q} w_m \mathbf{F}\left[\psi(\mathbf{x}, t^{n,m}); \mathbf{u}(\mathbf{x}, t^{n,m})\right], \quad (11)$$

where $\Delta t = t^{n+1} - t^n$, M_q denotes the number of points in the corresponding quadrature rule and

$$t^{n,m} = t^n + \frac{\Delta t}{2}(1 + \widetilde{x}_m). \quad (12)$$

An analogous formula to (11) is derived in RBS06 Eq. (13) for a modal basis. However, FF-SLSE differs from RBS06 in using a consistent high-order quadrature rule for all nodal points which is not influenced by the computed trajectories. This article proposes the use of the fourth-order accurate Simpson's rule for integration in time, which consists of nodal points and weights

$$\widetilde{x}_1 = -1, \qquad \widetilde{x}_2 = 0, \qquad \widetilde{x}_3 = 1, \quad (13)$$

$$w_1 = \tfrac{1}{6}, \qquad w_2 = \tfrac{2}{3}, \qquad w_3 = \tfrac{1}{6}. \quad (14)$$

All that now remains is to determine the pointwise fluxes as a function of the known state vector $\boldsymbol{\psi}^n$. Using the fact that tracer concentrations are transported with the flow, for a given $\mathbf{x}_i$ and t^{n+1} there exists some point $\mathbf{x}_i^*$ so that

$$q(\mathbf{x}_i, t^{n+1}) = q(\mathbf{x}_i^*, t^n). \quad (15)$$

The points $\mathbf{x}_i$ and $\mathbf{x}_i^*$ lie along the same fluid parcel trajectory, which is determined by the differential equation

$$\frac{d\mathbf{x}}{dt} = \mathbf{u}(\mathbf{x}, t), \quad (16)$$

for a sufficiently smooth velocity field $\mathbf{u}(\mathbf{x}, t)$. This equation is then solved subject to the condition $\mathbf{x}(t^{n+1}) = \mathbf{x}_i$. Equation (16) determines the trajectories of fluid particles, and can be solved using any standard numerical approach. When the velocity field is known in closed form, this equation can sometimes be integrated analytically to obtain $\mathbf{x}_i^*$. If the velocity field is only known at discrete points in time, this equation must instead be solved numerically. One such numerical approach for solving (16) uses a second-order two-stage Runge–Kutta scheme (Casulli, 1990; Giraldo, 1999; Rosatti *et al.*, 2005) of the form

$$\mathbf{x}_i^{(1)} = \mathbf{x}_i - \frac{(t - t^n)}{2} \mathbf{u}(\mathbf{x}_i, t), \quad (17)$$

$$\mathbf{x}_i^* = \mathbf{x}_i - (t - t^n)\mathbf{u}\left(\mathbf{x}_i^{(1)}, \frac{t + t^n}{2}\right). \quad (18)$$

Consequently the point $\mathbf{x}_i^*$ is an approximation to the point at time t^n, which under Lagrangian advection, would have ended up at $\mathbf{x}_i$ at time t. Curiously, even though $\mathbf{x}_i^*$ is only a second-order approximation to the exact trajectory origin, this choice does not appear to affect the spatial convergence rate of the underlying method. If higher accuracy and partial sub-stepping is desired for computing trajectories, a fourth-order Runge-Kutta scheme may

be applied, analogous to the one used by Ullrich *et al.* (2012),

$$\mathbf{x}_i^{(1)} = \mathbf{x}_i - \frac{(t - t^n)}{2}\mathbf{u}(\mathbf{x}_i, t), \tag{19}$$

$$\mathbf{x}_i^{(2)} = \mathbf{x}_i - \frac{(t - t^n)}{2}\mathbf{u}\left(\mathbf{x}_i^{(1)}, \frac{t + t^n}{2}\right), \tag{20}$$

$$\mathbf{x}_i^{(3)} = \mathbf{x}_i - (t - t^n)\mathbf{u}\left(\mathbf{x}_i^{(2)}, \frac{t + t^n}{2}\right), \tag{21}$$

$$\mathbf{x}_i^* = \frac{1}{3}\left(-\mathbf{x}_i + \mathbf{x}_i^{(1)} + 2\mathbf{x}_i^{(2)} + \mathbf{x}_i^{(3)}\right)$$
$$- \frac{(t - t^n)}{6}\mathbf{u}\left(\mathbf{x}_i^{(3)}, t^n\right). \tag{22}$$

However, for the tests considered in this article, the use of a higher-order trajectory computation scheme leads to nearly identical error norms (equal up to three decimal places). Other methods for solving (16) are also available (Durran, 1998; McGregor, 1993). Although the accuracy requirements for computing the trajectories do impose some additional expense, the corresponding trajectories must be computed only once per time step for all tracers. Once $\mathbf{x}_i^*$ is known, the pointwise flux is evaluated via

$$\mathbf{F}\left[\psi(\mathbf{x}_i, t^{n,m}); \mathbf{u}(\mathbf{x}, t^{n,m})\right]$$
$$= \mathbf{F}\left[q(\mathbf{x}_i^*, t^n)\rho(\mathbf{x}_i, t^{n,m}); \mathbf{u}(\mathbf{x}, t^{n,m})\right] \tag{23}$$
$$= q(\mathbf{x}_i^*, t^n)\rho(\mathbf{x}_i, t^{n,m})\mathbf{u}(\mathbf{x}_i, t^{n,m}).$$

The density $\rho(\mathbf{x}_i, t)$ is obtained from the dynamical core so as to ensure tracer–dynamics consistency.

It is worth observing that the trajectory computation presented above remains susceptible to crossed trajectories when the Lipschitz condition is not satisfied (Machenhauer *et al.*, 2009). This condition is far less strict than the Courant number restriction $\nu \leq 1$, and becomes an issue only in regions of very strong shear and/or divergence which rarely appear in the atmosphere. Nonetheless, to determine if crossed trajectories lead to an instability in FF-SLSE, a discontinuous velocity field was used to test advection of a Gaussian bell profile in 1D. By varying the strength of the discontinuity, it is easy to construct a situation where the CFL condition is satisfied but the field is arbitrarily divergent, and consequently trajectories were guaranteed to cross. However, in this situation, no evidence emerged of instability induced by crossed trajectories. Heuristically, this observation suggests that the use of trajectories to compute fluxes, as opposed to being used to obtain point values, may be more robust to crossed trajectories.

2.4. Time-integrated differential formulation of the spectral element method

An equivalent formulation of the spectral element method can be similarly obtained using spectral finite-differences. If the flux $\mathbf{F}(\mathbf{x}, t)$ is approximated via an expansion of basis functions ϕ_i,

$$\mathbf{F}(\mathbf{x}, t) = \sum_i \mathbf{F}\{\psi(\mathbf{x}_i, t); \mathbf{u}(\mathbf{x}_i, t)\}\phi_i(\mathbf{x}), \tag{24}$$

then (2) reduces to

$$\frac{\partial \psi}{\partial t} = -\sum_i \mathbf{F}\{\psi(\mathbf{x}_i, t); \mathbf{u}(\mathbf{x}_i, t)\} \cdot \nabla\phi_i(\mathbf{x}). \tag{25}$$

The update equation is then obtained by integrating this expression over the time interval $\mathcal{T}^n$ and evaluating the expression at $\mathbf{x} = \mathbf{x}_j$,

$$\widetilde{\psi}_j^{n+1} = \psi_j^n - \sum_i \overline{\mathbf{F}}^n(\mathbf{x}_i) \cdot \nabla\phi_i(\mathbf{x}_j). \tag{26}$$

At element boundaries where the basis functions are not differentiable, the derivatives $\nabla\phi_i(\mathbf{x}_j)$ are averaged among the one-sided derivatives on all intersecting elements. Consequently the differential formulation update equation (26) is identical to the variational form (9).

2.5. Stabilization and hyperdiffusion

The approach described in section 2.3 is consistent and ensures accuracy to high order, but exhibits instability for certain values of the Courant number (as will be demonstrated in section 3). This instability is removed via application of an explicit high-order numerical diffusion operator to filter out the unstable computational modes analogous to the approach of Taylor and Fournier (2010). As discussed by Pasquarelli and Quarteroni (1994), the application of diffusion is generally necessary for spectral approximations of advection–diffusion operators so as to remove spurious noise associated with the high-order basis functions. The diffusion operator is given by

$$\mathcal{H}^k\psi = \alpha \underbrace{(\nabla \cdot \nabla) \cdots (\nabla \cdot \nabla)}_{k \text{ times}} \psi = \alpha\nabla^{2k}\psi, \tag{27}$$

where α is the coefficient of diffusion and $2k \in \mathbb{Z}$ specifies the order of the diffusion operator. Note that, by applying the diffusion term to the tracer density, a very weak tracer–dynamics inconsistency is introduced; if desired, this can be avoided by applying an analogous diffusion operator to the density term after the thermodynamic update. The operator is applied using a forward Euler step, which is formulated as

$$\boldsymbol{\psi}^{n+1} = \widetilde{\boldsymbol{\psi}}^{n+1} + \Delta t \, \alpha \, \mathcal{H}^k \widetilde{\boldsymbol{\psi}}^{n+1}, \tag{28}$$

where $\widetilde{\boldsymbol{\psi}}^{n+1}$ is the updated tracer density following application of advection. The high-order Laplacian $\mathcal{H}^k$ is applied recursively by defining $\mathcal{H}^0\boldsymbol{\psi} = \widetilde{\boldsymbol{\psi}}^{n+1}$ and

$$\mathcal{H}^k\boldsymbol{\psi} = \mathcal{H}(\mathcal{H}^{k-1}\boldsymbol{\psi}) = \nabla \cdot \nabla(\mathcal{H}^{k-1}\boldsymbol{\psi}). \tag{29}$$

On applying the spectral-element discretization, as in section 2.2, along with expansion

$$\mathcal{H}^k\psi(\mathbf{x}, t) = \sum_j (\mathcal{H}^k\psi)_j(t)\,\phi_j(\mathbf{x}), \tag{30}$$

it follows that (29) can be written in matrix form as

$$\mathcal{H}^k\boldsymbol{\psi} = \mathbf{M}^{-1}\mathbf{H}(\mathcal{H}^{k-1}\boldsymbol{\psi}), \qquad (\mathbf{H})_{ij} = \int_{\mathcal{D}} \nabla\phi_i \cdot \nabla\phi_j \, \mathrm{d}V. \tag{31}$$

For example, the fourth-order diffusion operator can be applied via the three-stage procedure

$$\mathcal{H}\boldsymbol{\psi} = \mathbf{M}^{-1}\mathbf{H}\widetilde{\boldsymbol{\psi}}^{n+1}, \tag{32}$$
$$\mathcal{H}^2\boldsymbol{\psi} = \mathbf{M}^{-1}\mathbf{H}(\mathcal{H}\boldsymbol{\psi}), \tag{33}$$
$$\boldsymbol{\psi}^{n+1} = \widetilde{\boldsymbol{\psi}}^{n+1} + \Delta t \, \alpha \, \mathcal{H}^2\boldsymbol{\psi}. \tag{34}$$

2.6. Positivity preservation

The high-order nature of the method so far described does not guarantee positivity preservation. Further, unlike SEM, the FF-SLSE formulation does not satisfy a regularity condition on its fluxes which would ensure the total tracer mass within each spectral element remains positive. Hence, enforcement of the positivity condition is performed via a two-step process. First, FCT is applied during the flux computation stage to ensure that the total tracer mass within each spectral element is positive

after each time step. Edge fluxes into a spectral element Ω, with boundary $\partial\Omega$, are defined by observing

$$\langle\text{change in mass within }\Omega\rangle = \oint_{\partial\Omega} \mathbf{F} \cdot \mathbf{n}\, dS. \qquad (35)$$

That is, only fluxes computed at points along the boundary are responsible for changes to the total mass within each spectral element. With this in mind, FCT can be applied to limit pointwise fluxes at the element boundary analogous to the approach described by RBS06. For purposes of positivity preservation, the low-order flux required by FCT can simply be chosen to be the zero flux. Second, to ensure that the positivity criteria is retained within each spectral element, the optimal mass-borrowing scheme of Guba *et al.* (2013) is then applied. This scheme effectively identifies negative valued nodes within a spectral element and fills them using optimization within the same element.

Note that the fourth-order hyperdiffusion operator described in section 2.5 can also generate small spurious negative values when applied. Consequently, the hyperdiffusion operator is formulated in flux form by noting that the update equation (34) arises when $\mathbf{F}(\psi; \mathbf{u}) = \mathbf{F}_h(\psi) = \alpha\nabla(\mathcal{H}\psi)$ and (30) are substituted into (8).

Monotonicity preservation can be performed using an analogous procedure, except using a low-order flux to drive FCT. Strictly monotonic schemes tend to be overly diffusive when applied to tracer transport problems, and so the focus of this work is on methods which allow for small controlled overshoots (namely, total variation bounded schemes). One mechanism which seems to be very powerful for controlling overshoots in our approach simply limits the sample points $q(\mathbf{x}^*, t)$ in (23) to be bounded by all sample points within that spectral element. However, an analysis of this approach has not been pursued in detail.

2.7. Summary of the cubic scheme

This section provides an algorithmic outline of the FF-SLSE method with cubic basis functions. The basic algorithm used for advection is described as follows:

1. Backtrack trajectories from $\mathbf{x}_j$ and $t^{n,m}$ to obtain origin points $\mathbf{x}_j^*$ via (17)–(18);
2. Interpolate values of the tracer field via

$$q\left(\mathbf{x}_j^*, t^n\right) = \sum_i q_i^n \phi_i\left(\mathbf{x}_j^*\right); \qquad (36)$$

3. Calculate time-integrated fluxes $\overline{\mathbf{F}}^n(\mathbf{x}_j)$ via (11) and (23);

4. If flux-corrected transport is enabled, limit pointwise fluxes $\overline{\mathbf{F}}^n(\mathbf{x}_j)$;

5. Calculate predicted pointwise updates $\widetilde{\psi}_j^{n+1}$ via (9) or (26).

Once the advection step is completed, hyperdiffusion is then applied so as to ensure stability of the underlying scheme. This process proceeds as follows:

1. Calculate the Laplacian of the field following (32);

2. Compute hyperdiffusive fluxes

$$\mathbf{F}(\psi; \mathbf{u}) = \mathbf{F}_h(\psi) = \alpha\nabla(\mathcal{H}\psi); \qquad (37)$$

3. If flux-corrected transport is enabled, limit pointwise fluxes $\mathbf{F}(\mathbf{x}_j)$;

4. Calculate pointwise updates ψ_j^{n+1}.

3. 1D Analysis

A 1D dispersion analysis of FF-SLSE has been performed to determine the conditions required for stability of the method. Consider a single wave mode in 1D of the form

$$\psi(x, t) = \psi_0 \exp\{i(kx - \omega t)\}, \qquad (38)$$

with wave number k and frequency ω. For simplicity, density is assumed constant. Under the advection equation (2) with a constant uniform velocity field $u(x, t) = u_0 > 0$, this wave mode will propagate with dispersion relation $\omega = u_0 k$. The discrete setting instead leads to some approximate dispersion relationship $\overline{\omega} = \overline{\omega}(k)$, with $\overline{\omega}(k) \approx u_0 k$. Since $\overline{\omega}$ is complex-valued, the approximate dispersion relationship is typically decomposed into two terms: a normalized amplitude factor $A(k)$ defined by

$$A(k) = \exp\{T \cdot \text{Im}(\overline{\omega})\} \qquad (39)$$

and a normalized wave frequency

$$W(k) = T \cdot \text{Re}(\overline{\omega}). \qquad (40)$$

Hence, after a time T has elapsed, the wave mode will have amplitude $\psi_0 A(k)$ and will have shifted its phase by a factor $W(k)$. If the amplitude satisfies $A(k) > 1$ for any value k, this wave mode will grow in amplitude over time, and hence lead to an unstable numerical scheme. In the discrete domain, the dimensionless wave number $k\Delta x$ is typically adopted, which for resolvable wave modes spans the range $k\Delta x \in [0, \pi]$. For simplicity $T = 1$ time unit is chosen.

As an aside, note that Δx for nodal spectral element methods can be defined as either the width of each spectral element, or the average distance between nodes. The latter definition corresponds more closely with the concept of Δx being some inverse of the number of degrees of freedom present in the simulation. This article follows the approach of Giraldo and Restelli (2008), Dennis *et al.* (2012) and others, who use the average distance between nodes. In particular, this choice is important for our definition of the Courant number.

For the spectral element method, the non-uniform grid spacing leads to computational modes which are only approximately of the form (38). Nonetheless, most modes still exhibit wave-like character and can be analyzed in the context of standard dispersion theory. This analysis makes use of the dimensionless Courant number ν, defined by

$$\nu = \frac{u_0 \Delta t}{\Delta x}. \qquad (41)$$

In this article, the coefficient of diffusion α is chosen to take on the value which maintains stability of the method over the largest range of Courant numbers. For the method with cubic basis functions, this value, obtained from a simple grid search, turns out to be $\alpha = 3.4 \times 10^{-4} \Delta x^3$.

Figure 2 shows the normalized amplitude and frequency for all values of $k\Delta x$. Although the frequency is well captured by the numerical method, the scheme exhibits instability at $\nu = 0.3$ and $\nu = 2.1$. This instability is not associated with inaccuracies in the trajectory calculation, since it appears even in the 1D case when trajectories are computed exactly. In fact, the mild instability associated with $\nu = 0.3$ arises due to an inconsistency in the fluxes within a spectral element; namely, the time-averaged flux at the element boundary derives from the subgrid-scale reconstruction in the neighbouring spectral element, whereas all other time-averaged fluxes derive from the active spectral element. This inconsistency is small, but sufficient to drive instability in a small range of wave numbers. For larger Courant numbers (> 1.25), another inconsistency arises from the use of a single quadrature rule in time; that is, when computing time-averaged
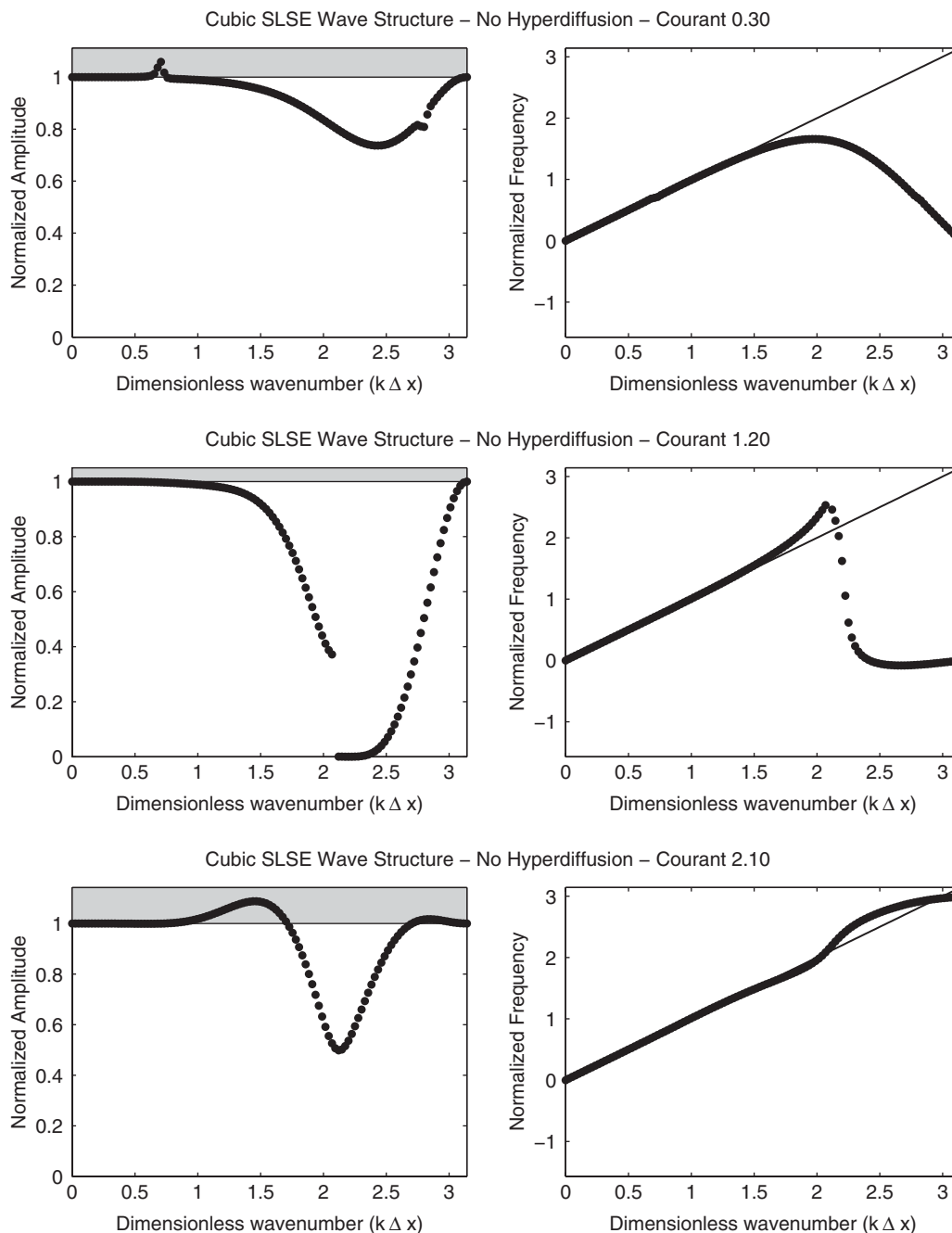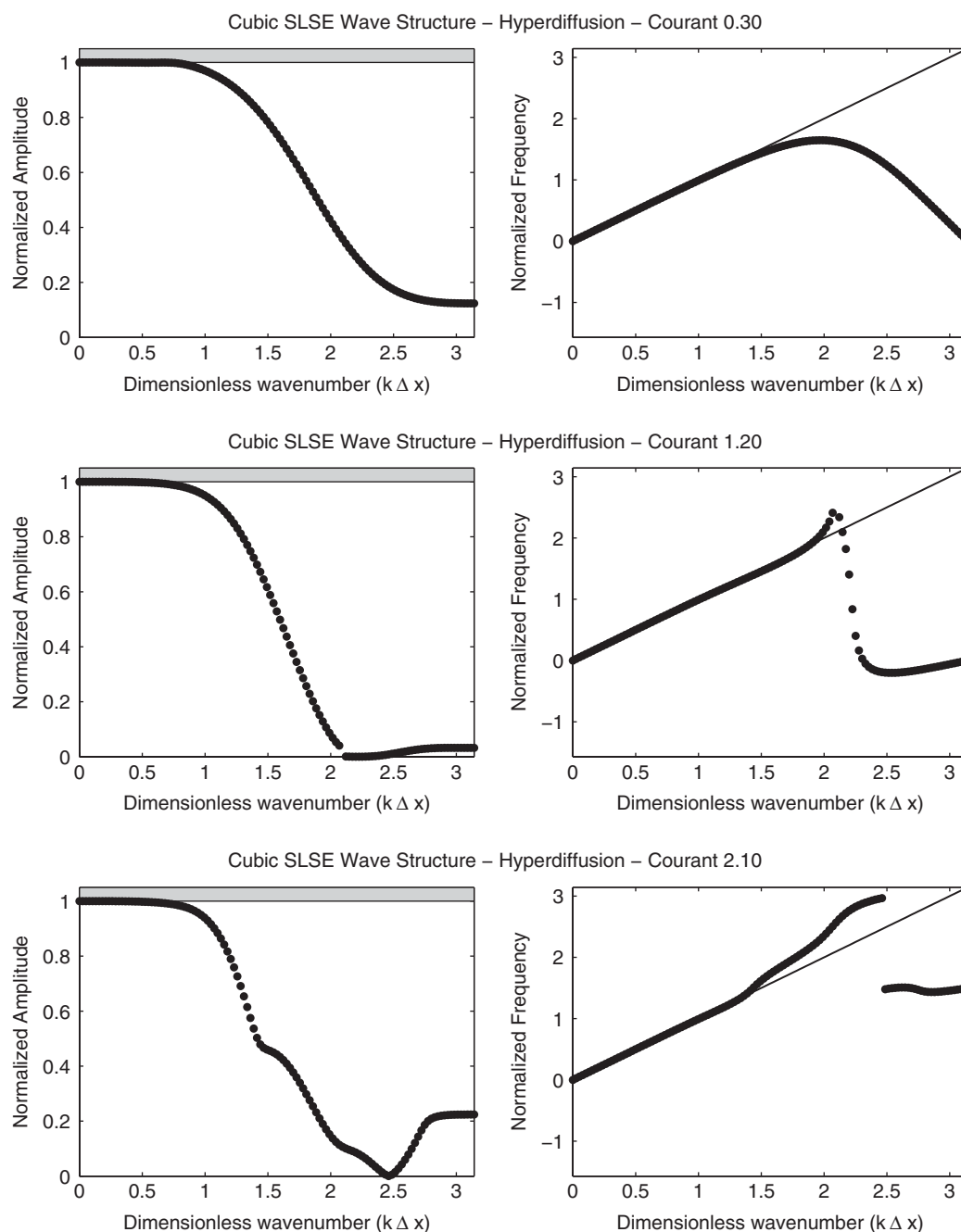
Figure 2. The cubic FF-SLSE method wave structure without added hyperdiffusion for (top) Courant number 0.3, (middle) Courant number 1.2 and (bottom) Courant number 2.1. For each value of the Courant number, the left plot shows the normalized amplitude and the right plot shows the normalized frequency. The grey region in the left plot depicts areas of instability. The straight line in the right plot shows the frequency for the exact scheme.

fluxes, the quadrature points in time could use information on q derived from multiple spectral elements. These instabilities are discussed in additional detail in the Appendix. Nonetheless, the addition of hyperdiffusion is effective at stabilizing the method, as shown in Figure 3. Again the frequency of each wave mode is well captured by the method, but in this case the amplitude $A(k)$ never enters the realm of instability. Figure 4 depicts the maximum value of the amplification factor over all resolved values of $k\Delta x$, and confirms that the approach with added hyperdiffusion is stable up to $\nu = 2.44$. Repeating this procedure for other choices of bases leads to Table 1. These results indicate that hyperdiffusion is needed only for basis functions of cubic order and higher. Further, there is a rapid loss of stability as the FF-SLSE scheme is applied to higher-order basis functions. Consequently the FF-SLSE method may not be desirable for schemes requiring greater than third-order accuracy.

4. Numerical results

This section provides a selection of 2D test cases to verify stability, robustness and accuracy of the FF-SLSE method described in this article. Uniform transport of a sinusoid is studied in section 4.1 to verify stability over long time integrations. Solid-body rotation tests are performed and analyzed in section 4.2. A deformational flow problem is presented in section 4.3 to test the method under a more complicated velocity field. Finally, a divergent flow problem is presented in section 4.4 to verify correct and consistent behaviour under divergent flow conditions. For the idealized tests presented in this article, it is assumed that the density is constant. The 2D Courant number used in the simulation description is defined as

$$\nu \equiv \max_{x,y \in \mathcal{D}} \frac{|\mathbf{u}(x,y)|\Delta x}{\Delta t}. \tag{42}$$

Figure 3. The cubic FF-SLSE method wave structure with added hyperdiffusion ($\alpha = 0.00034\Delta x^3$) for (top) Courant number 0.3, (middle) Courant number 1.2 and (bottom) Courant number 2.1. For each value of the Courant number, the left plot shows normalized amplitude and the right plot shows the normalized frequency. The grey region in the left plot depicts areas of instability. The straight line in the right plot shows the frequency for the exact scheme.
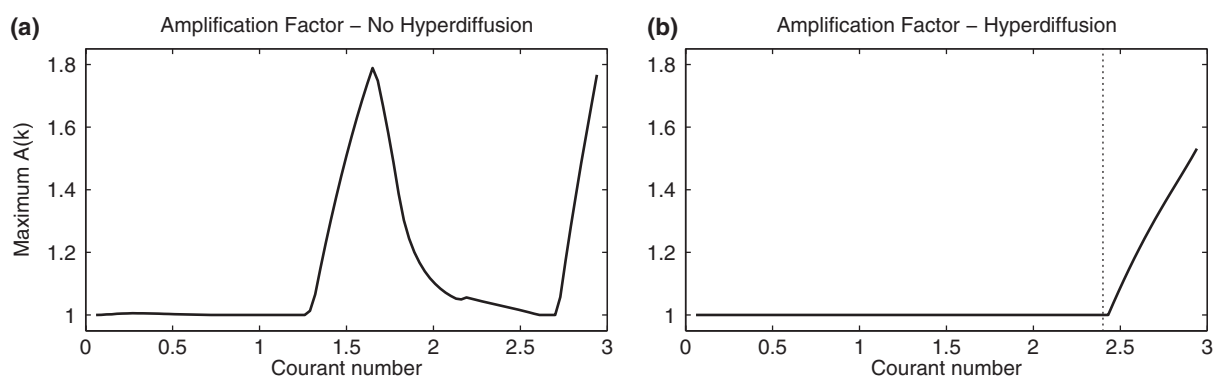
Figure 4. Maximum normalized amplification factor $A(k)$ over all resolved wave modes $k\Delta x \in [0, \pi]$ for the FF-SLSE method over cubic basis functions with values of the Courant number $\nu \in [0, 3]$. (a) shows the basic scheme with no added hyperdiffusion and (b) shows the scheme with added hyperdiffusion ($\alpha = 0.00034\Delta x^3$). The dotted line indicates the maximum stable Courant number for the scheme with hyperdiffusion, which occurs at $\nu = 2.44$.

Table 1. Maximum stable Courant number for various schemes.

Degree of basis	Hyperdiffusion type	α	Maximum Courant number
Linear (1)	None	–	1.00
Quadratic (2)	None	–	1.74
Cubic (3)	None	–	0.00
Cubic (3)	∇^4 hyperdiffusion	$3.4 \times 10^{-4}\ \Delta x^3$	2.44
Quartic (4)	∇^4 hyperdiffusion	$1.1 \times 10^{-4}\ \Delta x^3$	1.72
Quartic (4)	∇^6 hyperdiffusion	$-1.3 \times 10^{-6}\ \Delta x^5$	0.64
Quintic (5)	∇^6 hyperdiffusion	$-1.4 \times 10^{-7}\ \Delta x^5$	0.80
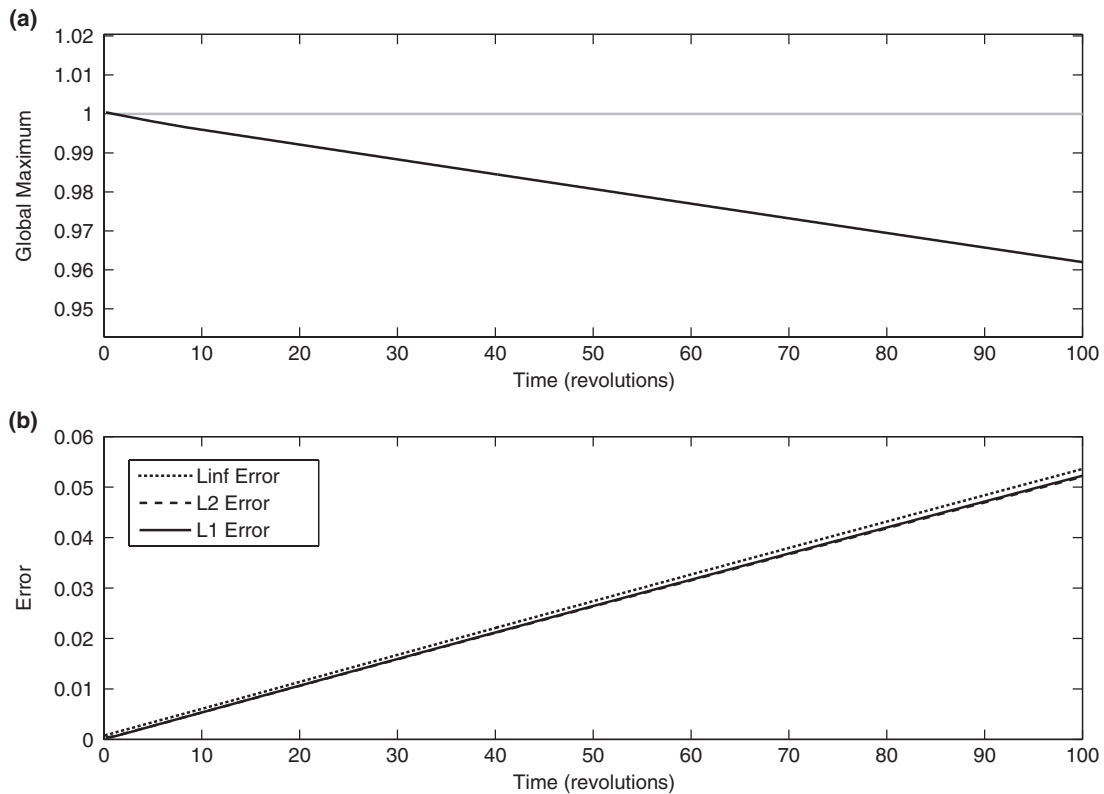
Figure 5. (a) Global maximum for the 2D uniform transport test, as a function of the number of revolutions completed by the test. The decaying profile suggests stability of the method. (b) Standard error norms for the profile over the duration of the simulation. The L_1 and L_2 errors are approximately equal and so are difficult to distinguish in this plot.

Throughout this section, standard error measures are used:

$$L_1(h) = \frac{I\left[|\psi - \psi_T|\right]}{I\left[|\psi_T|\right]}, \quad (43)$$

$$L_2(h) = \sqrt{\frac{I\left[(\psi - \psi_T)^2\right]}{I\left[\psi_T^2\right]}}, \quad (44)$$

$$L_\infty(h) = \frac{\max|\psi - \psi_T|}{\max|\psi_T|}, \quad (45)$$

where ψ_T is the tracer density at the initial time and I denotes an approximation to the global integral obtained by Gauss–Lobatto integration.

4.1. 2D uniform transport

The 2D uniform transport test is analogous to the 2D transport test of LeVeque (1986). This test uses a flow field of constant velocity, but transports the profile along a path which is not aligned with the grid. The flow field is chosen to be

$$u(x, y) = 1, \quad v(x, y) = 2. \quad (46)$$

A smooth initial profile

$$\psi(x, y) = \sin(2\pi x)\sin(2\pi y) \quad (47)$$

is used.

The test is run on a 10×10 mesh of spectral elements (total 30 nodes per coordinate direction) over the domain $\mathcal{D} = [0, 1]^2$ with a time step of $\Delta t = 0.02$ (Courant number 1.34) until $t = 100$. The global maximum and standard error norms are plotted for the duration of this simulation in Figure 5. The results show a monotone, linear decay in the global maximum, suggesting that the method is stable for the duration of this simulation. Error norms also increase linearly with time, as is expected for this simple transport experiment. At time $t = 1$, the L_2 error is approximately 4.73×10^{-4}, which is slightly better than the results from the third-order methods of LeVeque (1986).

4.2. 2D solid-body rotation

The 2D solid-body rotation test mimics the test case introduced by LeVeque (1986). The domain consists of the unit square $\mathcal{D} = [0, 1]^2$. The velocity field is given by

$$u(x, y) = -2\pi\left(y - \tfrac{1}{2}\right), \quad v(x, y) = 2\pi\left(x - \tfrac{1}{2}\right). \quad (48)$$

Although this definition leads to a discontinuity in the velocity field at the domain boundary, the tracer field is chosen to avoid impinging on the boundary for the duration of the simulation. This flow field is normalized such that one rotation is completed over an interval of 1 time unit.
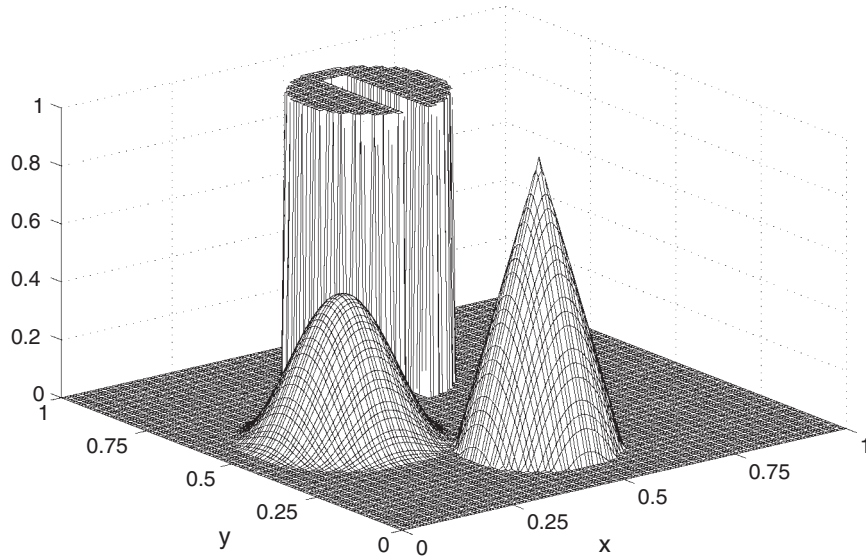
Figure 6. Initial data for the solid-body rotation test, showing tracer density $\psi(x, y)$ with 40×40 cubic spectral elements over the domain $(x, y) \in [0, 1]^2$ (total 120 nodes per coordinate direction).

Following LeVeque (1986), the tracer field consists of three shapes of variable smoothness to test various properties of the transport scheme. The initial data for this test is depicted in Figure 6. The first shape is a C^1 cosine bell centred at $(x_0^b, y_0^b) = (0.25, 0.5)$ with radius $r_0^b = 0.2$ and profile

$$\psi^b(x, y) = \begin{cases} \dfrac{1}{4}\left(1 + \cos\left(\dfrac{\pi r^b(\mathbf{x})}{r_0^b}\right)\right) & \text{if } r^b(\mathbf{x}) < r_0^b, \\ 0 & \text{otherwise.} \end{cases} \quad (49)$$

Here $r^b(\mathbf{x}) = \sqrt{(x - x_0^b)^2 + (y - y_0^b)^2}$ denotes the radius from the centre point of the bell. The second shape is a C^0 cone centred at $(x_0^c, y_0^c) = (0.5, 0.25)$ with radius $r_0^c = 0.15$ and profile

$$\psi^c(x, y) = \begin{cases} 1 - \dfrac{r^c(\mathbf{x})}{r_0^c} & \text{if } r^c(\mathbf{x}) < r_0^c, \\ 0 & \text{otherwise.} \end{cases} \quad (50)$$

Again $r^c(\mathbf{x}) = \sqrt{(x - x_0^c)^2 + (y - y_0^c)^2}$ denotes the radius from the centre point of the cone. The final shape is a discontinuous slotted cylinder centred at $(x_0^s, y_0^s) = (0.5, 0.75)$ with radius $r_0^s = 0.15$. The profile for the slotted cylinder is 1 for all points within r_0^s of the centre point, except for points that further satisfy

$$|x - x_0^s| < 0.025 \quad \text{and} \quad y < y_0^s + 0.1. \quad (51)$$

This test was run until $t = 1$ (one revolution) with a maximum Courant number of 2.4, which implies an approximate time step of $\Delta t = 0.006$ on a 20×20 mesh and $\Delta t = 0.003$ on a 40×40 mesh. Further, the positivity filter was employed to ensure no negative values emerged during the simulation. Results are shown in Figure 7 using a 20×20 mesh of spectral elements (total 60 nodes per coordinate direction) and in Figure 8 using a 40×40 mesh (total 120 nodes per coordinate direction). Overall there is very good agreement with the initial profile. No visual degradation of the cosine bell profile is observed after one revolution. On the other hand, there is a slight reduction in the height of the cone for both schemes, and a few visually apparent oscillations appear at the edge of the slotted cylinder. Nonetheless, on the 40×40 mesh the slotted cylinder is captured especially well, with very little sign of filling within the slot. Error norms associated with these results are given in Table 2 for all objects, as well as isolated errors for each object. Consistent

Table 2. Error norms for the 2D solid body rotation test with all three objects (All), only the C1 cosine bell (Bell), only the C0 cone (Cone) and only the discontinuous slotted cylinder (S.Cyl.).

Test	Mesh size	L_1 error	L_2 error	L_∞ error
All	20×20	2.60 (-2)	9.67 (-2)	8.09 (-1)
	40×40	1.45 (-2)	6.70 (-2)	9.08 (-1)
	80×80	8.92 (-3)	5.28 (-2)	9.52 (-1)
Bell	20×20	2.07 (-4)	6.65 (-4)	6.14 (-3)
	40×40	3.65 (-5)	1.28 (-4)	1.01 (-3)
	80×80	7.30 (-6)	2.92 (-5)	3.53 (-4)
Cone	20×20	1.48 (-3)	5.89 (-3)	1.49 (-1)
	40×40	5.21 (-4)	2.35 (-3)	8.26 (-2)
	80×80	1.81 (-4)	9.45 (-4)	4.57 (-2)
S.Cyl.	20×20	2.44 (-2)	9.70 (-2)	8.08 (-1)
	40×40	1.38 (-2)	6.71 (-2)	9.07 (-1)
	80×80	8.50 (-2)	5.28 (-2)	9.52 (-1)

with other Eulerian transport schemes, the discontinuous profile shows no convergence in the L_∞ norm, whereas the cone and bell exhibit approximately first- and second-order convergence in this norm (and better performance in L_1 and L_2). The errors in the full simulation are largely overwhelmed by the errors due to the slotted cylinder. To demonstrate that mass is conserved throughout the simulation, we plot the mass difference over time in Figure 9, defined by

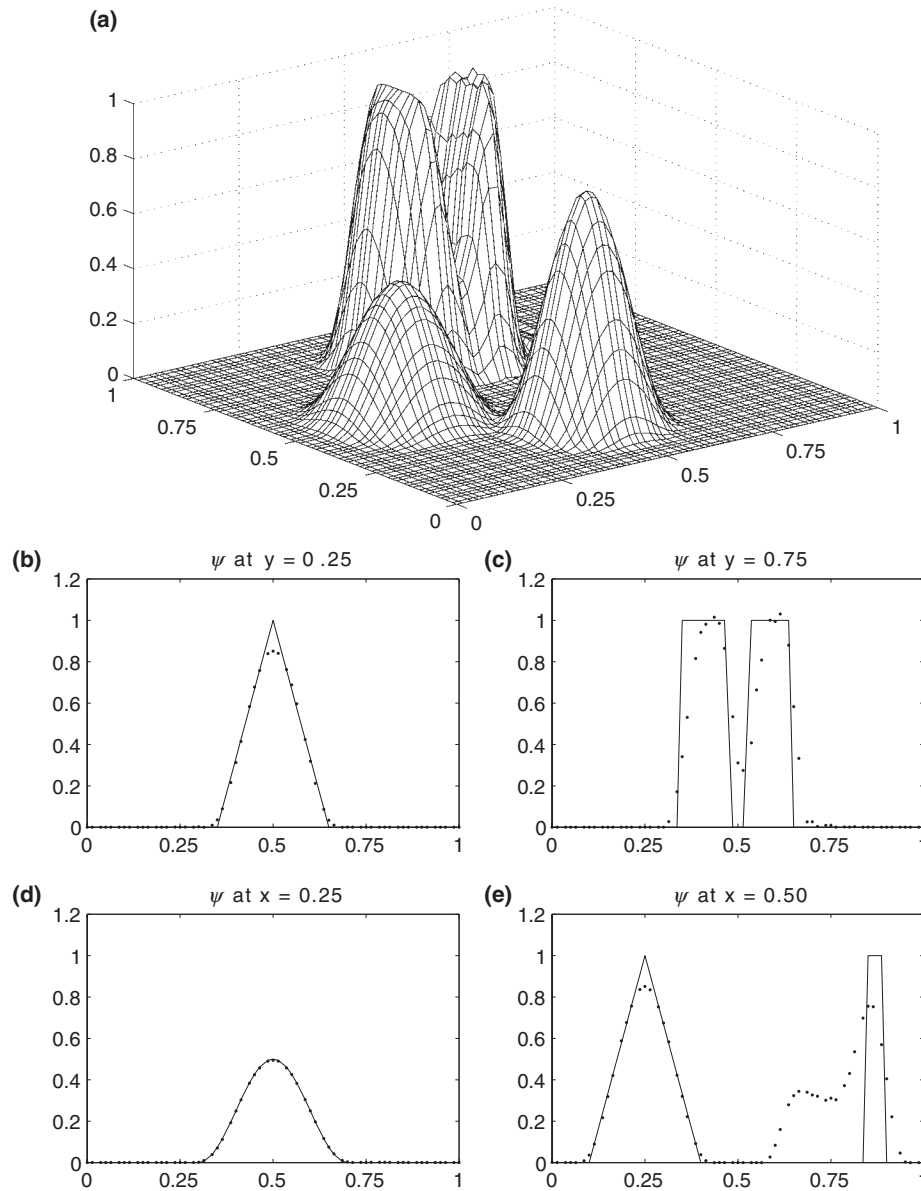$$\Delta M^n = M^n - M^0, \quad \text{with } M^n = \int_{\mathcal{D}} \psi^n(x, y) \, \mathrm{d}V, \quad (52)$$

where the integral is evaluated on the spectral element mesh.

4.3. 2D deformational flow

The 2D deformational flow test is again based on the work of LeVeque (1986), and is useful for evaluating the treatment of thin filaments within the advection scheme. The 2D non-divergent velocity field is specified as

$$u(x, y, t) = \sin^2(\pi x) \sin(2\pi y) \cos(\pi t/T), \quad (53)$$

$$v(x, y, t) = -\sin^2(\pi y) \sin(2\pi x) \cos(\pi t/T), \quad (54)$$

(a)

(b) ψ at y = 0 .25

(c) ψ at y = 0.75

(d) ψ at x = 0.25

(e) ψ at x = 0.50

Figure 7. Results from the solid-body rotation test after one revolution, showing tracer density $\psi(x, y)$ on a 20×20 cubic spectral element mesh (total 60 nodes per coordinate direction) with $\Delta t = 0.006$. (a) shows a 3D surface view of the tracer density. The lower plots show four different cross-sections at (b) $y = 0.25$, (c) $y = 0.75$, (d) $x = 0.25$ and (e) $x = 0.5$. The solid lines depicts the exact solutions.

where $\mathcal{D} = [0, 1]^2$ and the final time is $T = 5$ time units. The initial distribution is chosen to be a C^3 cosine bell, defined by

$$\psi(x, y) = \frac{1}{4} [1 + \cos(\pi r)]^2, \tag{55}$$

$$\text{with} \quad r = \min \left\{ 1, 4 \left[\left(x - \tfrac{1}{4} \right)^2 + \left(y - \tfrac{1}{4} \right)^2 \right]^{1/2} \right\}.$$

This distribution is chosen over the standard C^1 cosine bell since the latter allows at most second-order convergence of the error norms. Over the duration of the test, the cosine bell is deformed to a narrow stretched band at $t = T/2$, at which point the flow reverses and (optimally) the tracer field will return to its initial distribution (Durran, 1998).

This test case was run with and without the positivity filter described in section 2.6. On the 40×40 mesh of spectral elements (120 total nodes in each coordinate direction) the time step was chosen to be $\Delta t = 0.01$ which corresponds to a Courant number of $\nu = 1.2$. The results from this test are plotted in Figure 10. The filter is clearly effective at removing spurious negative values from the results, although it has the effect of also somewhat degrading the quality of the solution. Further, the scheme appears effective at maintaining the tracer field even when it has been stretched to a very thin filament a few grid points across.

Error norms with and without the positivity filter are plotted in Figure 11. Below a mesh resolution of 40×40, the filament is not resolved on the grid at $t = T/2$, and so sub-optimal convergence is observed. However, at higher resolutions the method is attaining third-order convergence, as expected from the analysis in section 3. The filter degrades the errors slightly over the unfiltered scheme, but still leads to convergence at roughly third-order.

4.4. 2D divergent flow

A new 2D divergent flow test has been formulated to demonstrate that this method can be used even for divergent flow fields. The basic flow field is closely modelled after the divergent flow test of (Nair and Lauritzen, 2010), except modified for Cartesian geometry. It consists of a divergent component overlaid on top of a steady flow in the positive x direction,

$$u(x', y', t) = -\sin^2\left(\frac{x'}{2}\right) \sin y' \cos^2 y' \cos\left(\frac{\pi t}{T}\right) + \frac{1}{T}, \tag{56}$$

$$v(x', y', t) = \frac{1}{2} \sin x' \cos^3 y' \cos\left(\frac{\pi t}{T}\right), \tag{57}$$

(a)

(b)
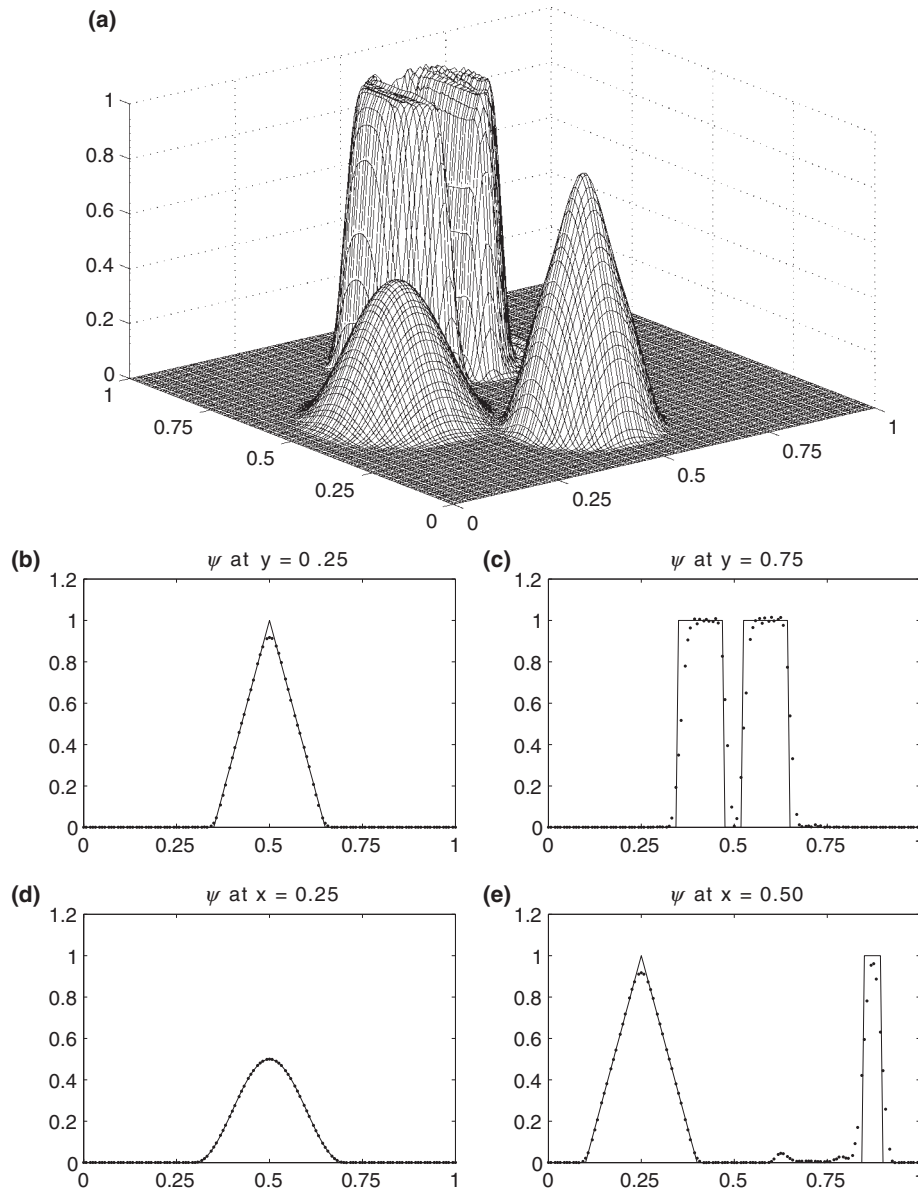

(c)

(d)

(e)

Figure 8. As Figure 7, but run on a 40×40 mesh (total 120 nodes per coordinate direction) with $\Delta t = 0.003$.
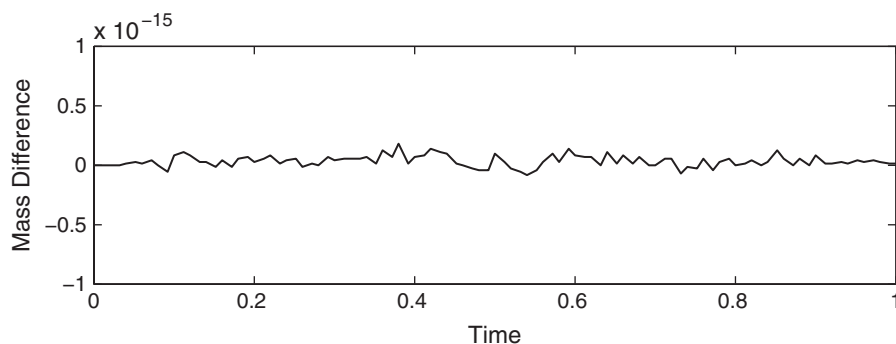

Figure 9. Mass difference from the solid body rotation test on a 40×40 mesh over the duration of the simulation. All errors are within machine truncation.

where

$$x' = 2\pi \left(x - \frac{t}{T}\right), \qquad y' = \pi \left(y - \frac{1}{2}\right), \qquad (58)$$

where $T = 1$ is the period of the flow. Since the divergent component of the flow reverses exactly over one period, the final state of the tracer field should match exactly with the initial state. The domain is the unit square $\mathcal{D} = [0, 1]^2$ with periodic boundary conditions in all directions. The tracer field consists of two C^3 cosine bells, centred at $(x_1, y_1) = (0.25, 0)$ and $(x_2, y_2) = (0.75, 0)$
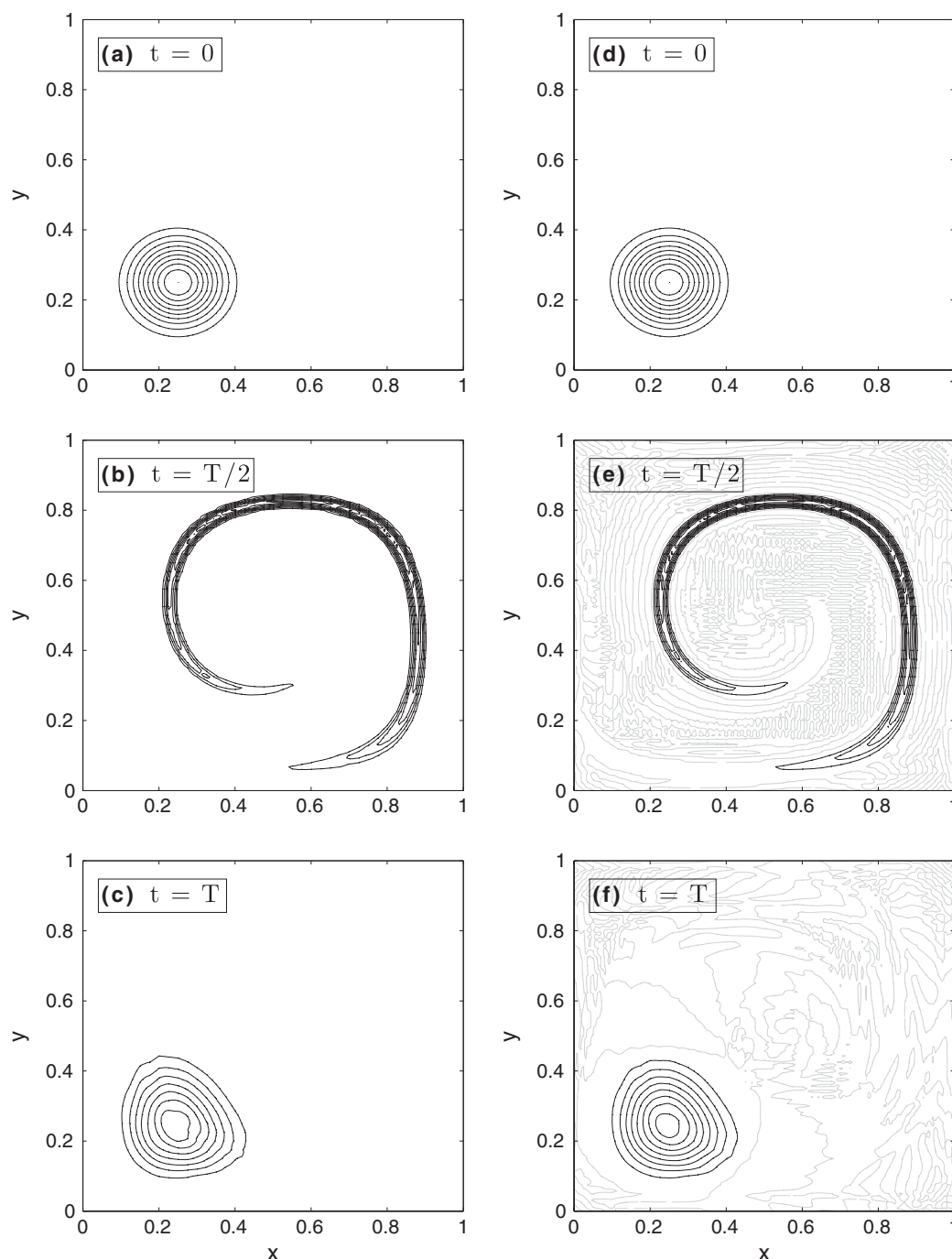
with radius $R = 0.35$,

$$\psi_i(x, y) = \begin{cases} \frac{1}{4} \left[1 + \cos\left(\frac{\pi r_i}{R}\right)\right]^2 & \text{if } r_i < R, \\ 0 & \text{otherwise,} \end{cases} \qquad (59)$$

where

$$r_i = \sqrt{(x - x_i)^2 + (y - y_i)^2}, \qquad (60)$$

so that the total tracer density is given by $\psi(x, y) = \psi_1(x, y) + \psi_2(x, y)$. Since the flow field is divergent, it is no longer
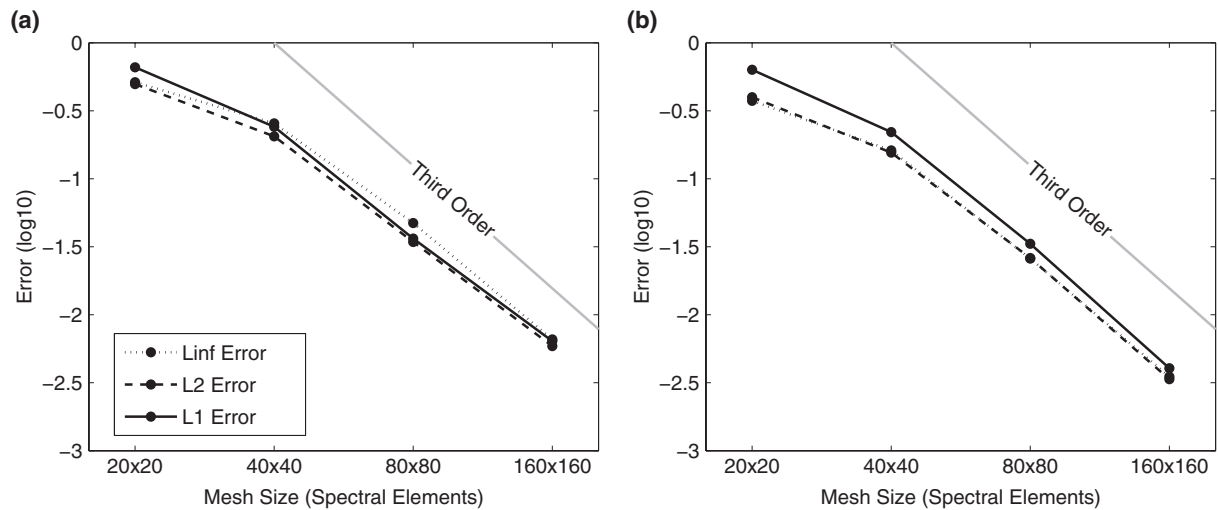
Figure 10. Results from the deformational flow test with (a, b, c) the filtered scheme and (d, e, f) the unfiltered scheme on a 40×40 mesh (120 total nodes in each coordinate direction) with $\Delta t = 0.01$ ($\nu = 1.2$). Results are shown at (a, d) the initial time $t = 0$, (b, e) maximum deformation $t = T/2$ and (c, f) the final time $t = T$. The zero line is depicted in grey.

appropriate to approximate the density field as constant in space and time. To simulate coupling with a dynamically evolved density field, a fourth-order spectral-element method with Runge--Kutta time integrator is used to solve the continuity equation with an initially constant density field. The coupling procedure is described in section 2. The results of this test are depicted in Figure 12 for a 40×40 mesh (120 nodes total in each coordinate direction) with $\Delta t = 0.006$. The tracer field reaches maximum deformation at time $t = T/2$, where the divergence of the flow field has enhanced ψ to approximately 2.38. To verify that convergence holds for the divergent flow field, error norms have been plotted in Figure 13 for meshes from 20×20 elements (60 nodes total in each coordinate direction) to 160×160 elements (480 nodes in each coordinate direction). The method is super-convergent for low resolutions at around fourth-order accuracy, but eventually exhibits asymptotic third-order convergence in all norms.

5. Conclusions

This article has presented a Flux-Form Semi-Lagrangian Spectral Element (FF-SLSE) method for conservative tracer transport on the nodal spectral element grid. In particular, this scheme differs from other semi-Lagrangian finite-element methods by ensuring exact conservation in a nodal framework without any imposition on the character of the velocity field. This approach addresses many of the known issues with tracer transport using the standard spectral element method; in particular, the small time step restriction is loosened with fewer parallel communications. The proposed approach computes time-integrated fluxes at GLL nodes to obtain pointwise updates, and so does not require potentially complicated area integration. Since the method is formulated in flux-form, the spectral element method also guarantees exact conservation of tracer mass. Time-integrated fluxes are computed using a combination of backwards trajectories and Simpson's rule,

Figure 11. Log_{10} plot of the error norms from the deformational flow test with (a) the filtered scheme and (b) the unfiltered scheme (the values a along the y-axis denote 10^a). Mesh resolution is varied with a constant Courant number 1.20, corresponding to $\Delta t = 0.01$ at 40×40 resolution. The straight grey line shows third-order convergence.
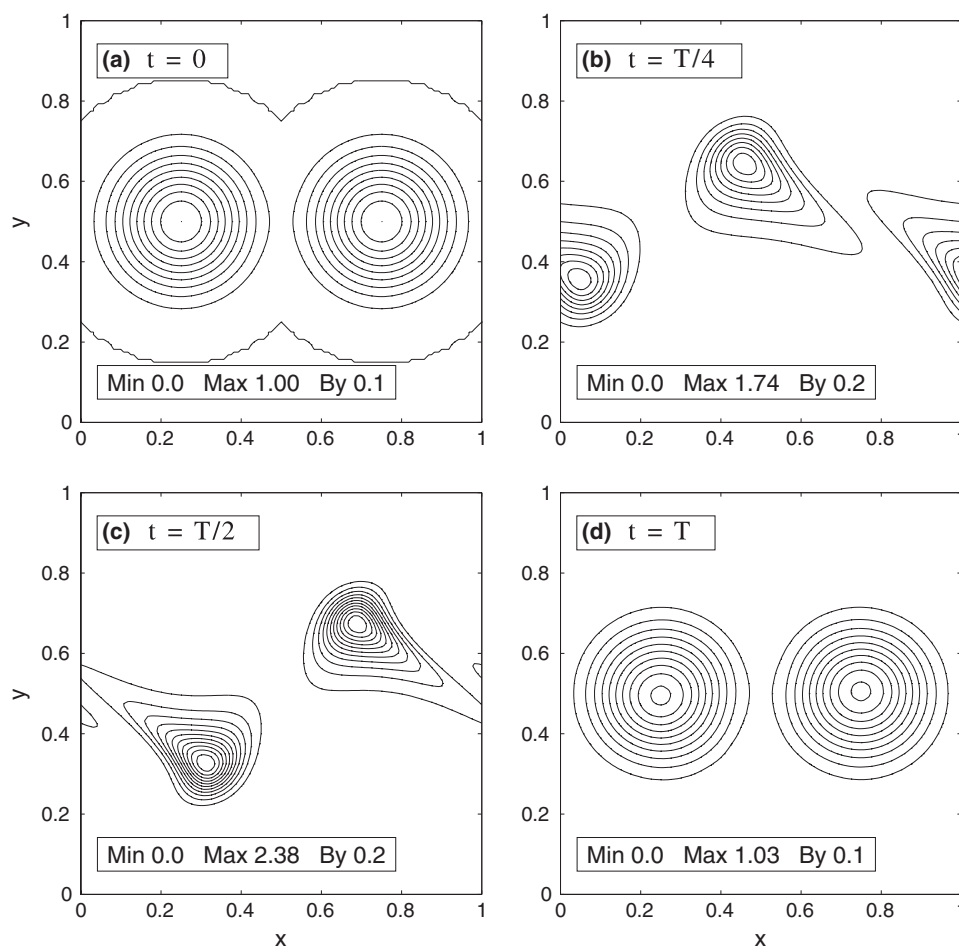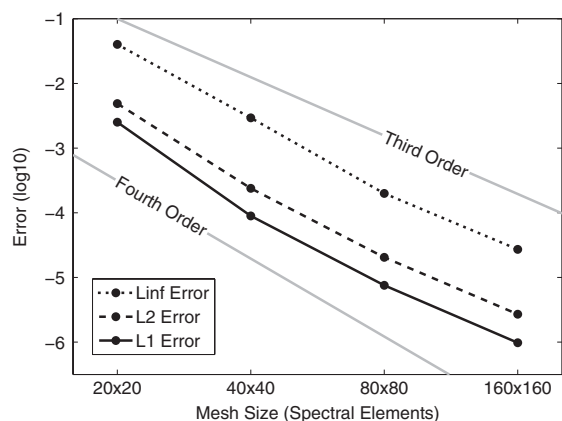

Figure 12. Results from the divergent flow test at time (a) $t = 0$, (b) $t = T/4$, (c) $t = T/2$, (d) $t = T$, showing tracer density $\psi(x, y)$ on a 40×40 cubic spectral element mesh with $\Delta t = 0.006$. The contour interval is 0.1 for plots (a) and (d) and 0.2 for plots (b) and (c).

so as to ensure at least fourth-order accuracy with the base scheme. Although the base scheme exhibits mild instability, the instability can be controlled with the application of ∇^4 hyperdiffusion with a coefficient which scales at $O(\Delta x^3)$. Consequently the scheme with cubic basis functions exhibits third-order convergence on sufficiently smooth problems, matching the approach currently used in the spectral element dynamical core. A positivity filter is also presented which is effective at removing spurious negative values using a combination of flux-corrected transport and local optimized filtering. The positivity filter can be extended to impose strict monotonicity as well, although this approach was not

pursued here. By using the native spectral element grid, issues which may arise due to remapping between the dynamics and tracer grid are avoided and optimal parallel scalability of the underlying method is retained.

Several numerical tests have been performed to verify stability, accuracy, conservation and robustness of the method. These tests include transport, solid body rotation, deformational flow and divergent flow in 2D and are useful for verifying the theoretical properties of the method under a variety of flow situations. As expected, third-order convergence of the method is observed when hyperdiffusion is applied and a sufficiently smooth tracer

Figure 13. Log_{10} plot of the error norms from the divergent flow test after one period with variable grid resolution and filtering (the values a along the y-axis denote 10^a). Mesh resolution is varied with a constant Courant number 1.50, corresponding to $\Delta t = 0.006$ at 40×40 resolution.

field is used. The positivity filter has also been verified to remove spurious negative values without greatly affecting the quality of the solution.

This article argues that this scheme is effective for an accurate, efficient treatment of atmospheric transport problems. In the future it is expected that this scheme will be incorporated into the CAM spectral element dynamical core as an alternative method for tracer transport.

Acknowledgements

Appendix

Understanding the 1D semi-Lagrangian instability

This appendix addresses the observed instability in the FF-SLSE method in the 1D case, which imposes the need for an explicit hyperdiffusion operator to ensure stability. Specifically, the instability can be traced back to two approximations which, in the variational formulation, have been made in evaluating

the space–time integral on the right-hand side of (5). Both approximations are associated with the use of a quadrature rule to integrate the 2D space-time flux (Figure A.1∗), which is discontinuous in its first derivative along the characteristic which passes through the element boundary (the corner characteristic). The first approximation, here denoted Approximation A, uses a single quadrature rule in space (here we have used GLL quadrature) to integrate over the time-averaged fluxes $\overline{\mathbf{F}}^n$ in each element j. In the differential formulation (section 2.4) this approximation is equivalent to expanding the flux using the GLL basis functions in (24). The second approximation, here denoted Approximation B, is associated with the quadrature in time and only appears when the Courant number is sufficiently large for the characteristic to bisect the quadrature of $\mathbf{F}$ (performed via Simpson's rule) which is used to compute $\overline{\overline{\mathbf{F}}}^n$ at each GLL node.

To remove the instability associated with Approximation A, the spatial quadrature can be separated into two regions aligned with the corner characteristic (Figure A.1(a)). Using this approach, the amplification factor is recalculated and plotted in Figure A.2(a). The modification has an immediate and dramatic effect on the amplification factor, leading to a drop from a maximum of 1.8 for $\nu \leq 2.5$ (Figure 4) to 1.001 and a removal of the mild instability around $\nu = 0.3$.

To remove the instability associated with Approximation B, all fluxes which are bisected by the corner characteristic are evaluated using separate quadrature rules (Figure A.1(b)). Using this approach, the amplification factor is recalculated and plotted in Figure A.2(b). This modification reduces the amplification factor to approximately 1.1, but retains a tri-modal instability structure. However, this approach is also stable for all $\nu \in [0, 3]$ when hyperdiffusion is applied.

Finally, to remove both approximations, the integration procedure is formulated to separate both spatial and temporal integration (Figure A.1(c)). The amplification factor is again recalculated and plotted in Figure A.2(c), leading to a scheme which is stable for all $\nu \in [0, 3]$ (and hence unconditionally stable in 1D), even without the application of hyperdiffusion. Since the flux integral is evaluated exactly, this unapproximated scheme is equivalent to a flux-form formulation of a remapping scheme.

In 2D, these approximations are more difficult and costly to overcome in practice. In this case Approximation B is likely the easiest to remove, by detecting when backwards-traced characteristics intersect with the element boundary. However, a modification to remove Approximation A would effectively require a search algorithm to detect overlapped areas, which would increase the complexity of the underlying method.
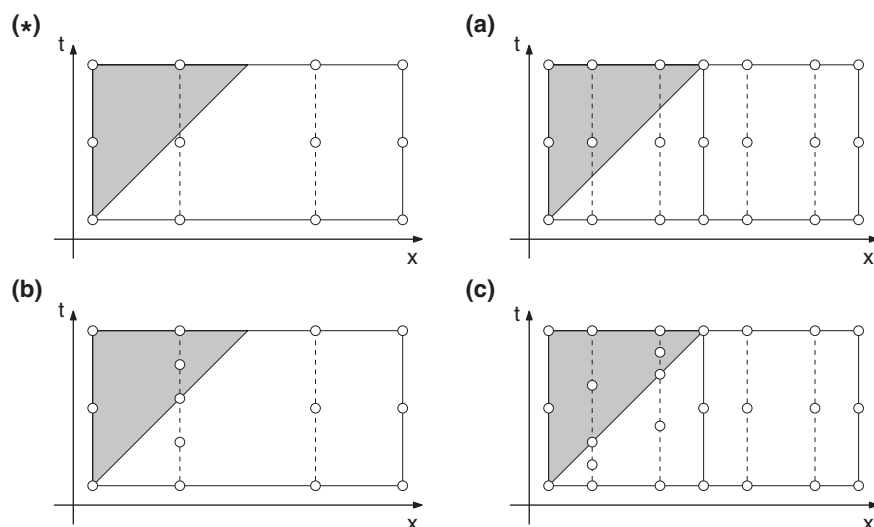
Figure A.1. Four approaches for evaluating the flux integral in (5) over a single element j. The diagonal line denotes a characteristic which passes through the left-most point of element j at the initial time and so represents a discontinuity in the first derivative of the tracer density ψ. Consequently, the shaded region uses flux information from the element immediately to the left (element $j - 1$), whereas the white region derives flux information from element j. The open circles denote points where the flux is evaluated as part of the integration procedure.
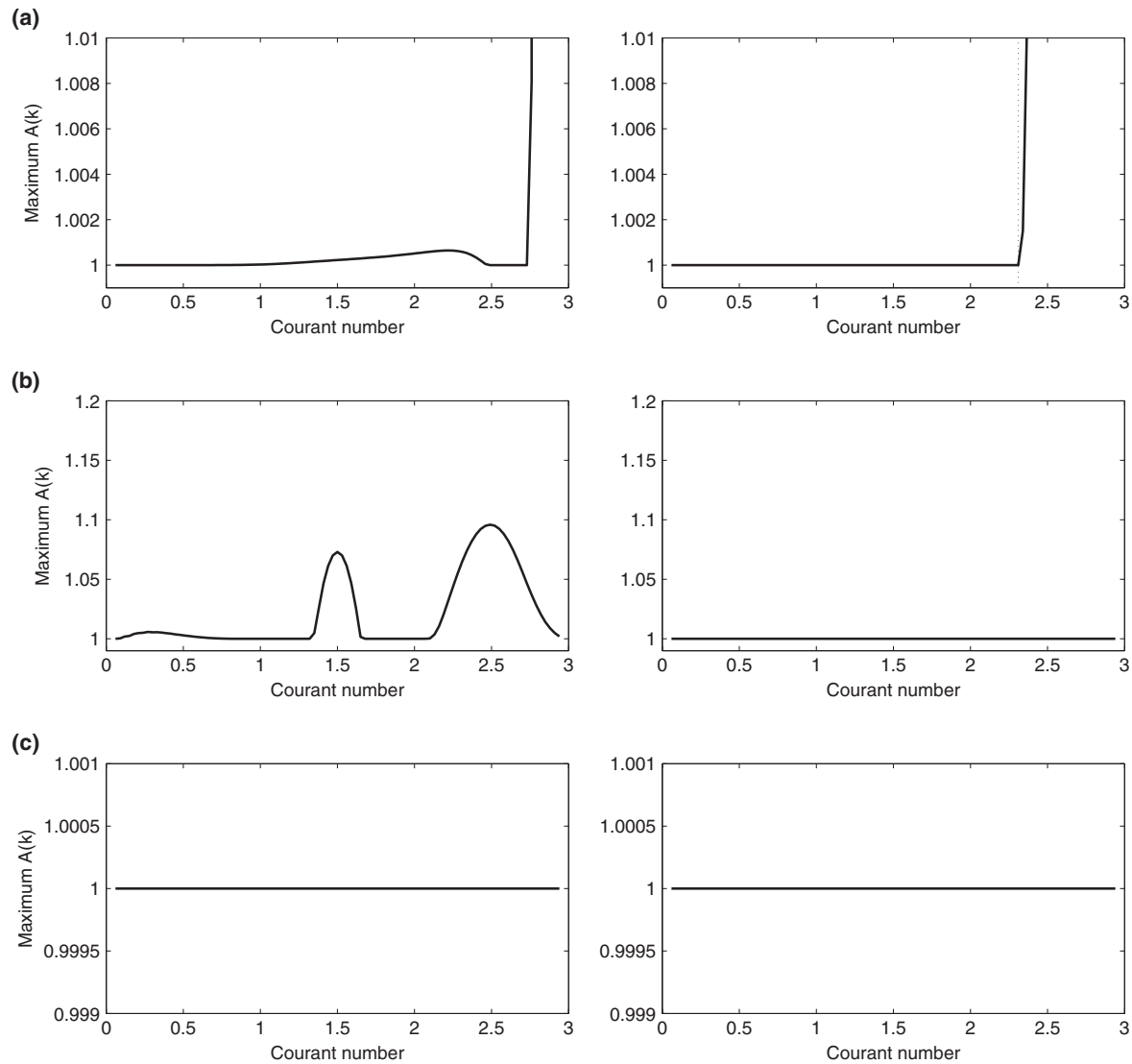
Figure A.2. Maximum normalized amplification factor $A(k)$ over all resolved wave modes $k\Delta x \in [0, \pi]$ for various modified versions (see text) of the FF-SLSE method over cubic basis functions with values of the Courant number $\nu \in [0, 3]$. The left plots shows the basic scheme with no added hyperdiffusion and the right plots shows the scheme with added hyperdiffusion ($\alpha = 0.00034\Delta x^3$). The dotted line indicates the maximum stable Courant number for the scheme with hyperdiffusion. Note the range of the y-axis is different for each case.

References

Barth TJ, Jespersen DC. 1989. The design and application of upwind schemes on unstructured meshes. In *Proc. AIAA 27th Aerospace Sciences Meeting*, Reno, NE.

Casulli V. 1990. Semi-implicit finite difference methods for the two-dimensional shallow-water equations. *J. Comput. Phys.* **86**: 56−74.

Cockburn B, Shu CW. 1989. TVB Runge−Kutta local projection discontinuous Galerkin finite element method for conservation laws. II: General framework. *Math. Comput.* **52**: 411−435.

Colella P, Woodward PR. 1984. The piecewise parabolic method (PPM) for gas-dynamical simulations. *J. Comput. Phys.* **54**: 174−201.

Dennis J, Edwards J, Evans KJ, Guba ON, Lauritzen PH, Mirin AA, St-Cyr A, Taylor MA, Worley PH. 2012. CAM-SE: A scalable spectral element dynamical core for the Community Atmosphere Model. *Int. J. High Perform. Comput. Appl.* DOI: 10.1177/1094342011428142.

Durran DD. 1998. *Numerical Methods for Wave Equations in Geophysical Fluid Dynamics*. Springer-Verlag: Berlin.

Fournier A, Taylor MA, Tribbia JJ. 2004. The Spectral Element Atmosphere Model (SEAM): High-resolution parallel computation and localized resolution of regional dynamics. *Mon. Weather Rev.* **132**: 726−748.

Frolkovič P. 2002. Flux-based method of characteristics for contaminant transport in flowing groundwater. *Comput. Visual. Sci.* **5**: 73−83.

Giraldo FX. 1998. The Lagrange−Galerkin spectral element method on unstructured quadrilateral grids. *J. Comput. Phys.* **147**: 114−146.

Giraldo FX. 1999. Trajectory calculations for spherical geodesic grids in Cartesian space. *Mon. Weather Rev.* **127**: 1651−1662.

Giraldo FX, Restelli M. 2008. A study of spectral element and discontinuous Galerkin methods for the Navier−Stokes equations in non-hydrostatic mesoscale atmospheric modeling: Equation sets and test cases. *J. Comput. Phys.* **227**: 3849−3877.

Giraldo FX, Rosmond TE. 2004. A Scalable Spectral Element Eulerian Atmospheric Model (SEE-AM) for NWP: Dynamical Core Tests. *Mon. Weather Rev.* **132**: 133−153.

Giraldo FX, Perot JB, Fischer PF. 2003. A spectral element semi-Lagrangian (SESL) method for the spherical shallow-water equations. *J. Comput. Phys.* **190**: 623−650.

Guba ON, Taylor MA, St-Cyr A. 2013. Optimal limiters for the spectral element method. *J. Comput. Phys.* submitted.

Harris LM, Lauritzen PH, Mittal R. 2011. A flux-form version of the conservative semi-Lagrangian multi-tracer transport scheme (CSLAM) on the cubed sphere grid. *J. Comput. Phys.* **230**: 1215−1237.

Hirt CW, Amsden AA, Cook JL. 1974. An arbitrary Lagrangian−Eulerian computing method for all flow speeds. *J. Comput. Phys.* **14**: 227−253.

Laprise JP, Plante A. 1995. A class of semi-Lagrangian integrated-mass (SLM) numerical transport algorithms. *Mon. Weather Rev.* **123**: 553−565.

Lauritzen PH, Nair RD, Ullrich PA. 2010. atlA conservative semi-Lagrangian multi-tracer transport scheme (CSLAM) on the cubed-sphere grid. *J. Comput. Phys.* **229**: 1401−1424.

Lauritzen PH, Erath C, Mittal R. 2011a. On simplifying 'incremental remap'-based transport schemes. *J. Comput. Phys.* **230**: 7957−7963.

Lauritzen PH, Ullrich PA, Nair RD. 2011b. Atmospheric transport schemes: Desirable properties and a semi-Lagrangian view on finite-volume discretizations. Chapter 8 in *Numerical Techniques for Global Atmospheric Models*. Lecture Notes in Computational Science and Engineering. **80**: 185−250. Lauritzen PH, Jablonowski C, Taylor MA, Nair RD. (eds) Springer: Berlin.

Leonard BP, Lock AP, MacVean MK. 1996. Conservative explicit unrestricted-time-step multidimensional constancy-preserving advection schemes. *Mon. Weather Rev.* **124**: 2588−2606.

Leslie LM, Purser RJ. 1995. Three-dimensional mass-conserving semi-Lagrangian scheme employing forward trajectories. *Mon. Weather Rev.* **123**: 2551–2566.

LeVeque RJ. 1996. High-resolution conservative algorithms for advection in incompressible flow. *SIAM J. Numer. Anal.* **33**: 627–665.

Lin S-J, Rood RB. 1996. Multidimensional flux-form semi-Lagrangian transport schemes. *Mon. Weather Rev.* **124**: 2046.

Ma H. 1993. A spectral element basin model for the shallow-water equations. *J. Comput. Phys.* **109**: 133–149.

Machenhauer B, Kaas E, Lauritzen PH. 2009. Finite volume methods in meteorology. *Comput. Methods Atmos. Ocean.* **761**: Handbook of Numerical Analysis.

Maday Y, Patera AT. 1989. Spectral element methods for the incompressible Navier–Stokes equations. In *State-of-the-art surveys on computational mechanics.* (A90-47176 21-64) Amer. Soc. Mech. Eng: New York, 71–143.

McGregor JL. 1993. Economical determination of departure points for semi-Lagrangian models. *Mon. Weather Rev.* **121**: 221–230.

Nair RD, Lauritzen PH. 2010. A class of deformational flow test cases for linear transport problems on the sphere. *J. Comput. Phys.* **229**: 8868–8887.

Nair RD, Scroggs JS, Semazzi FHM. 2002. Efficient conservative global transport schemes for climate and atmospheric chemistry models. *Mon. Weather Rev.* **130**: 2059–2073.

Norman MR, Nair RD. 2008. Inherently conservative nonpolynomial-based remapping schemes: Application to semi-Lagrangian transport. *Mon. Weather Rev.* **136**: 5044–5061.

Pasquarelli F, Quarteroni A. 1994. Effective spectral approximations of convection-diffusion equations. *Comput. Method Appl. Math.* **116**: 39–51.

Patera AT. 1984. A spectral element method for fluid dynamics: Laminar flow in a channel expansion. *J. Comput. Phys.* **54**: 468–488.

Prather MJ. 1986. Numerical advection by conservation of second-order moments. *J. Geophys. Res.* **91**: 6671–6681.

Purser RJ, Leslie LM. 1991. An efficient interpolation procedure for high-order three-dimensional semi-Lagrangian models. *Mon. Weather Rev.* **119**: 2492–2498.

Rančic M. 1992. Semi-Lagrangian piecewise biparabolic scheme for two-dimensional horizontal advection of a passive scalar. *Mon. Weather Rev.* **120**: 1394–1406.

Restelli M, Bonaventura L, Sacco R. 2006. A semi-Lagrangian discontinuous Galerkin method for scalar advection by incompressible flows. *J. Comput. Phys.* **216**: 195–215.

Rosatti G, Cesari D, Bonaventura L. 2005. Semi-implicit, semi-Lagrangian modelling for environmental problems on staggered Cartesian grids with cut cells. *J. Comput. Phys.* **204**: 353–377.

Staniforth A, Côté J. 1991. Semi-Lagrangian integration schemes for atmospheric models – a review. *Mon. Weather Rev.* **119**: 2206–2223.

Taylor MA, Fournier A. 2010. A compatible and conservative spectral element method on unstructured grids. *J. Comput. Phys.* **229**: 5879–5895.

Taylor MA, Tribbia J, Iskandarani M. 1997. The Spectral Element Method for the shallow-water equations on the sphere. *J. Comput. Phys.* **130**: 92–108.

Ullrich PA, Lauritzen PH, Jablonowski C. 2012. Some considerations for high-order 'incremental remap'-based transport schemes: edges, reconstructions, and area integration. *Int. J. Numer. Meth. Fluids* DOI: 10.1002/fld.3703.

Xiu D, Karniadakis GE. 2001. A semi-Lagrangian high-order method for Navier–Stokes equations. *J. Comput. Phys.* **172**: 658–684.

Zalesak ST. 1979. Fully multidimensional flux-corrected transport algorithms for fluids. *J. Comput. Phys.* **31**: 335–362.

Zerroukat M, Wood N, Staniforth A. 2002. SLICE: A Semi-Lagrangian Inherently Conserving and Efficient scheme for transport problems. *Q. J. R. Meteorol. Soc.* **128**: 2801–2820.

Zerroukat M, Wood N, Staniforth A. 2004. SLICE-S: A Semi-Lagrangian Inherently Conserving and Efficient scheme for transport problems on the Sphere. *Q. J. R. Meteorol. Soc.* **130**: 2649–2664.